Modeling and Design of Magnetic Flux Compression Generators

by

Nicholas Edward Klugman
B.S. in Electrical Science and Engineering and in Mathematics,
Massachusetts Institute of Technology (2019)

Submitted to the Department of Electrical Engineering and Computer Science
in partial fulfillment of the requirements for the degree of
Master of Engineering in Electrical Engineering and Computer Science
at the
MASSACHUSETTS INSTITUTE OF TECHNOLOGY
February 2020

Author .....
Department of Electrical Engineering and Computer Science
January 8, 2020

Certified by .....
Jeffrey Lang
Professor
Thesis Supervisor

Certified by .....
James Vedral
Principle Member of the Technical Staff, Draper
Thesis Supervisor

Accepted by .....
Katrina LaCurts
Chair, Master of Engineering Thesis Committee

Modeling and Design of Magnetic Flux Compression Generators

by

Nicholas Edward Klugman

Submitted to the Department of Electrical Engineering and Computer Science
on January 8, 2020, in partial fulfillment of the
requirements for the degree of
Master of Engineering in Electrical Engineering and Computer Science

Abstract

The explosively-pumped magnetic flux compression generator (FCG) is a pulsed-power current amplifier powered by an explosion. This thesis surveys FCGs, demonstrating their general operation; develops a new magnetic-field-strength-based model for FCGs in the form of a generalized cylinder that more accurately captures losses to magnetic diffusion than commonly employed circuit models, but maintains simplicity in the form of a low order DAE; develops a simplified means of calculating the inductance of FCGs, providing a bridge between the field-based and circuit models; presents a design of a full loop FCG system (a topology underserved by existing literature) and an experimental setup to verify the designed loop generator; and proposes a class of non-explosive magnetic flux compression generators. The designs and models herein provide new tools and jumping-off points for further research into FCGs, particularly in the miniaturized systems gaining popularity and in the potential for reusable flux compression power sources.

Thesis Supervisor: Jeffrey Lang
Title: Professor

Thesis Supervisor: James Vedral
Title: Principle Member of the Technical Staff, Draper

Acknowledgments

I would like to thank the following, whose contributions were essential to the success of this project:

James Vedral for providing daily advisement and introducing me to flux compression generators.

Jeffrey Lang for advising the project and providing the inspiration for the magnetic-field-based model developed herein (as well as teaching me the physics involved in this project during my undergraduate education).

Carlos Rodriguez for sharing his expertise in explosives, a field previously unknown to me, but essential to this project.

Giselle Ventura and Daniel Lang for their efforts on the mechanical side of the project, including the CADs of Chapter 6.

Charles Stark Draper Laboratories for providing the resources for this project.

My entire family for supporting me and encouraging me throughout my entire life.

Aletheia Church for providing a family in Boston and reminding me how to do all work as for my Savior, Jesus Christ.

Contents

List of Figures

Chapter 1

Introduction

For applications ranging from radar to nuclear fusion to lasers and beyond, delivering high peak power for a short duration (pulsed power) is an essential capability. Developed in 1950s simultaneously by the United States and the former Soviet Union, the explosively pumped magnetic flux compression generator (FCG) provides pulsed power by harnessing the potential chemical energy of high explosives and converting it into magnetic field energy. By compressing magnetic flux from a seed current source, an FCG provides gain in both current and internal magnetic field strength. Flux compression generators have been used in high power microwave sources, high power lasers, plasma focus machines, plasma guns, X-ray sources, particle accelerators, rail guns, very high magnetic field research, and fusion research [1]. They have produced megagauss magnetic fields, several hundred megampere currents [2], and peak power in excess of 10 GW [3]. Until relatively recently, research into FCGs focused on increasing gain or final magnetic field strength. Some more recent efforts have attempted to miniaturize the technology, creating a portable, small-scale pulsed power source [4]–[6].

Renewed interest in these generators in recent years [1], [7] motivates both new designs and updated models [8], [9] for FCGs. Additionally, limited efforts have been made to produce a non-explosive flux compression generator [10]. Should a non-explosive FCG be developed that operates at lower speeds, flux loss to diffusion would assume a greater role and modeling such a device would require closer attention to

flux loss dynamics than the equivalent circuit models usually employed.

This thesis develops a new model for flux compresion generators, placing greater emphasis on the dynamics of diffusive flux loss, while still remaining a simple model; presents a design for a full flux compression system, including the seed current source and experimental setup; and proposes a new, non-explosive flux compression generator design.

This thesis is structured as follows: after giving a brief review of FCG operating principles and common topologies (Chapter 2), Chapter 3 develops a magnetic-field-strength-based model for FCGs that focuses on accurately tracking flux losses to diffusion (with means of calculating inductance of FCGs presented in the Appendix to bridge the gap between the field-based model and the current-based model more useful in some pulsed-power applications). Following this is a design of a seed current source and description of other possible sources that are commonly employed (Chapter 4), as well as a design of a loop flux compression generator and accompanying experiment to test the operation of the device (Chapter 5). In Chapter 6, a non-explosive means of flux compression utilizing deployable structures is proposed, Finally, Chapter 7 subsists of a summary, conclusions, and suggestions for future work.

Chapter 2

Background

This chapter provides background information on explosively-pumped magnetic flux compression generators, first by explaining their basic operating premise, then by reviewing seven common generator topologies. The chapter concludes with an explanation of the choice of the loop generator for the design in Chapter 5. This thesis abbreviates explosively-pumped magnetic flux compression generators as FCGs or generators (though at times others also use EPFCG, MFCG, and MCG, the last of which occurs particularly often in Soviet/Russian literature, compared to the FCG acronym more common in American literature) [1]. For an introduction to various explosive pulsed power technologies, including FCGs, see [7] and for a thorough review of FCGs see [1]. The classic text on FCGs is [11], which treats the topic in some depth, even taking at times a more pure electromagnetics perspective. A more modern text is [12], which was published to include the thirty years of results following [11], but focuses on the helical FCG at the expense of other topologies (though this could also be said of the general corpus of literature on FCGs). This thesis (in Chapter 3) presents a model of flux compression generators simpler and in some cases more practically useful than the models of [11] that provide similarly rigorous attention to the effects of magnetic diffusion, but with greater attention to this phenomenon than the circuit equivalent models of [1] or even [12].

2.1 General FCG Operation

FCGs operate on the premise of flux conservation — the flux in a shorted inductor will remain constant, neglecting resistive losses. By rapidly decreasing the area of (or number of turns in) the inductor, the magnitude of the magnetic fields piercing that area will increase accordingly to conserve flux. Equivalently, decreasing the inductance rapidly increases the current. Put another way, FCGs operate similar to inverse rail guns. Rail guns use high current and high magnetic fields to launch a projectile; FCGs "launch a projectile" using explosives and convert that kinetic energy into electromagnetic energy in the form of high current and high magnetic fields. Since an FCG requires an initial flux (or equivalently an initial current), it operates as high-power current amplifier, requiring a seed current source. Historically, this source has been a capacitor bank, but in recent history newer, explosively-powered pulsed-current sources have been used (see [7] for information on such sources and [13] for an example of such a source powering an FCG).

Mathematically, the flux in a single-turn inductor is given by $\Lambda = Li = BA$, where L is the inductance, i is the current, A is the area, and B is the average field strength. Neglecting resistive losses, when the inductor is shorted the flux is Λ throughout operation, regardless of mechanical alterations made. So, decreasing the area from A_i to A_f increases the magnetic field from $B_i = \Lambda/A_i$ to $B_f = \Lambda/A_f$. Thus, the magnetic field experiences a gain of $B_f/B_i = A_i/A_f$. For long, single-turn inductors, the inductance is given by $L = \mu A/l$, where μ is the magnetic permeability of the core and l is the length of the inductor. Therefore, decreasing the area decreases the inductance. (The inductance of a solenoid is given by $L = \mu n^2 Al$, where n is the turn density, so decreasing the length of a solenoid while maintaining the turn density decreases its inductance.) So, we also consider decreasing the inductance from L_i to L_f, which increases the current from $i_i = \Lambda/L_i$ to $i_f = \Lambda/L_f$. In this case, the current experiences a gain of $i_f/i_i = L_i/L_f$. The energy stored in the inductor increases from $U_i = \Lambda^2/(2L_i)$ to $U_f = \Lambda^2/(2L_f)$, with an energy of $\Delta U = \left(L_f^{-1} - L_i^{-1}\right)\Lambda^2/2$ captured from the explosion. When the generator has a purely

inductive load, it is sufficient to add the inductance of the load to the initial and final generator inductances when calculating L_i and L_f, respectively. For resistive and capacitive loads, equivalent circuits are often employed; a thorough analysis of the different cases, including different means of connecting the load, is given in Chapter 5 of [12].

To familiarize ourselves intuitively with the operation of flux compression generators, we consider several different configurations: the plate generator, the cylindrical implosion generator, the loop generator, the strip generator, the coaxial generator, the disk generator, and finally the helical generator. These generators are ordered so as to highlight similar operation between the designs and how one might use one topology as inspiration for designing another (for example, the coaxial generator is presented as a rotation of the strip generator). Indeed, this review is not intended to be a resource for deciding between these generator topologies for any given application or list of requirements (for this purpose, see [1], [14]), but rather an introduction for someone with little-to-no experience with FCGs to understand the general operating principles of flux compression generators by highlighting the structural similarities and differences of these generators and their mechanism of flux compression. Information on the different generator types is from [1], [14], unless otherwise stated.

2.2 Plate Generator

In the case of the plate generator, the current discharged from the capacitor bank flows from the input through two parallel plates into the load, pictured in Figure 2-1 as the loop on the right. When current flows through the device, magnetic fields are generated within the device, pointing into the paper. The parallel plates are lined with high explosive (HE) on the exterior, such that upon detonation the plates move together, shorting (and thereby isolating) the input, and decreasing the area through which the magnetic fields flow. (The explosive is generally timed so that the input is cut off at the moment of peak current.) Intuitively speaking we can imagine the plates squeezing the magnetic flux into the output cavity, increasing the flux there

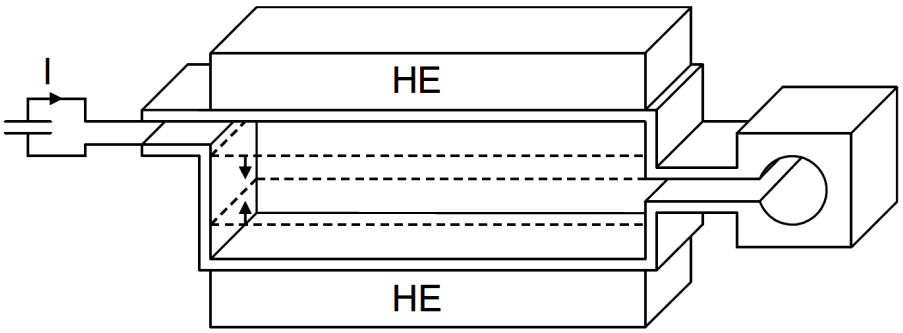

Figure 2-1: Plate Generator. The high explosives (HE) seal the input (pictured left) and bring the top and bottom plates together, forcing the flux into the output coil (pictured right). Image from [14].

and the current through the output conductor.

More formally, the inductance of the FCG inductor is $L = \mu A/w$, where μ is the magnetic permeability of the space between the plates, A is the area pierced by the magnetic field, and w is the depth of the device (the dimension parallel to the magnetic field). The area is decreasing, so the inductance is as well. Since flux is conserved and $\lambda = Li$ (where λ is the flux and i is the current), decreasing the inductance generates a corresponding increase in current.

The plate generator has a relatively simple construction and is rugged "with some reservation," however it requires simultaneous detonation of the explosive across the surface, which requires more expensive detonators [1]. The depth determines the current-carrying capacity, which is generally very high.

2.3 Cylindrical Implosion Generator

The cylindrical implosion generator works in a manner similar to plate generator. Imagine extending and adding a curvature to the top plate such that it contacts itself, forming a cylinder, while removing the bottom plate which would have been inside the cylinder. We now have a cylindrical cavity surrounded by explosives, as shown in Figure 2-2. Often to generate a magnetic field inside of the cavity, external coils are wrapped around the cylinder, which carry current and induce a current in

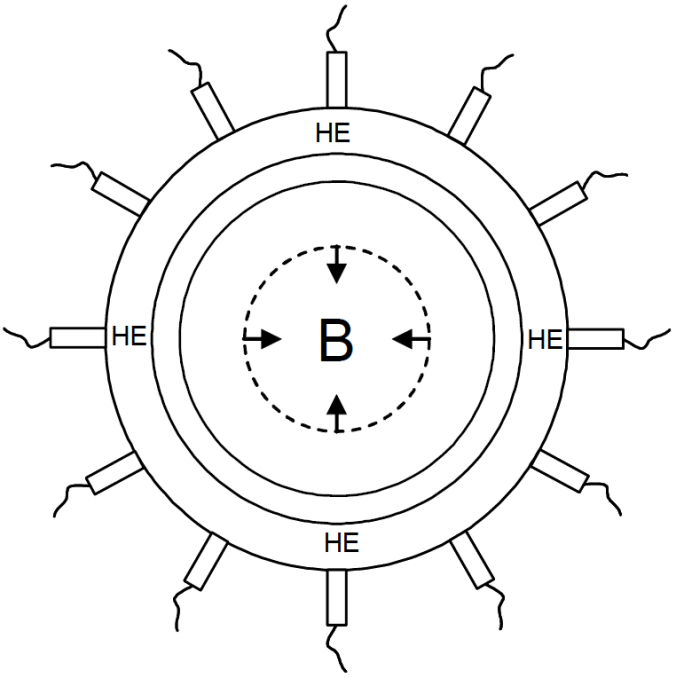

Figure 2-2: Cylindrical Implosion Generator. Simultaneous detonation of the high explosive (HE) compresses the volume in which the magnetic flux resides, increasing the magnetic field strength. Image from [14].

the cylinder. The flux is now similarly compressed when the explosives are detonated simultaneously (note that such detonators would be expensive). In these generators magnetic fields in excess of 10 MG have been reported. Indeed, the pressure from the magnetic field is at times great enough to stop the implosion and even turn around the imploding cylinder before the cylinder is completely destroyed.

2.4 Loop Generator

The loop generator is similar to an inside-out version of the cylindrical implosion generator. The outer conducting cylinder (known as the stator) has two slits cut in it (one for the input and one for the output), as shown in Figure 2-3. The inner cylinder (known as the armature) is filled with explosives. Upon detonatin, the inner cylinder expands, decreasing the volume that the magnetic fields can occupy, thus decreasing the inductance. When the explosives are detonated, the area pierced by the magnetic fields (which go into the page) decreases. The amature is off-center so

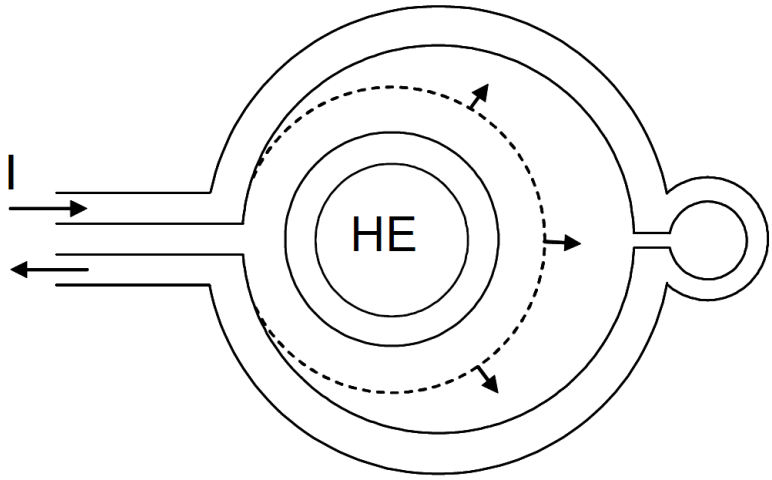

Figure 2-3: Loop Generator. Detonation of the high explosive (HE) causes the armature to expand, shrinking the cavity between it and the stator, forcing the flux into the output coil (pictured right). Image from [14].

that the explosion causes it to short the input, cutting it off so that flux is conserved in the device.

This generator's simple design provides it with a relatively low production cost and lends itself to sturdy construction. The loop generator also has relatively high volume energy density and surface current density, allowing approximately 70% of kinetic energy to be converted into electromagnetic engergy [12]. It is also accomadating to a wide range of load inductances. This generator is designed to make a large magnetic field in a small volume and multiple are easily connected in series or parallel, though they provide relatively low current gain (often between 7 and 10). The loop generator is less present in literature than many of the other topologies mentioned in this chapter. Indeed, while [13] in 2007 claims that the loop FCG was invented ten years prior, [1] credits Lukasik with the first description of this topology in 1965 in [15], which demonstrates how little this topology was explored in the thirty years following its invention.

Magnetic fields within loop generators have reached 133 T and currents in the 50 MA range have been demonstrated.

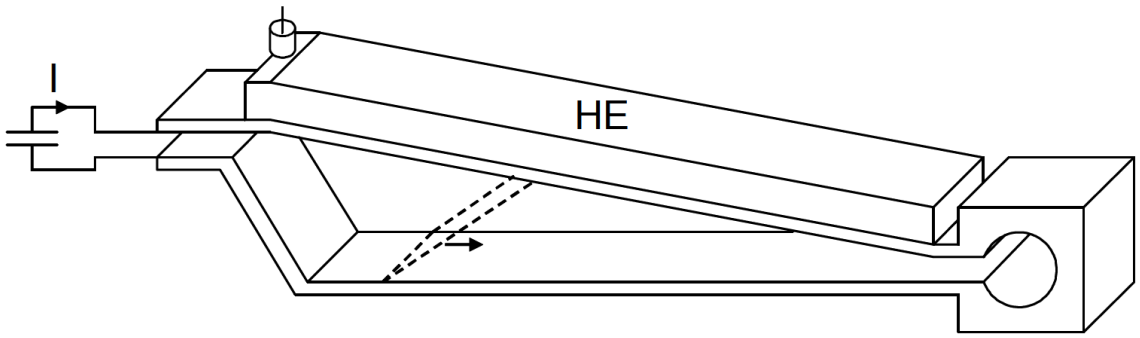

Figure 2-4: Strip Generator. As the high explosive (HE) detonates from left to right (input to output), the flux-containing cavity decreases in volume, forcing the flux into the output coil (pictured right). Image from [14].

2.5 Strip Generator

Unlike the previous generators, the strip generator does not require simultaneous detonation, making it less expensive to fabricate. Detonation begins on the input side, as shown in Figure 2-4. At detonation the input is shorted and flux becomes conserved in the system. The top plate folds and slides along the bottom plate, decreasing the area of the device, increasing the magnetic field and the current. This device shares the plate generator's capability of carrying current (megampere peak values), but is flimsier, being limited by the force of magnetic pressure within the device.

2.6 Coaxial Generator

The coaxial generator resembles a rotation of the strip generator about an axis going through the explosive from input to output. The magnetic field now wraps around the inner conducting cylinder (known as the armature) in the cavity between it and the outer conducting cylinder (known as the stator), as the current flows through the stator to the output (not pictured in Figure 2-5) and back from output to input through the armature. The detonation still proceeds from input to output, cutting off the input while shorting the armature to the stator. As the conical front approaches the output, the area between the armature and the stator decreases, once again

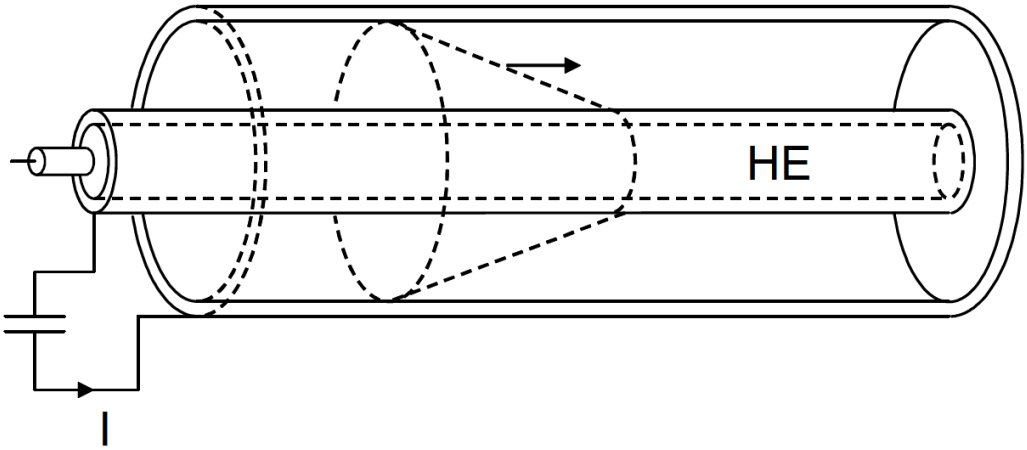

Figure 2-5: Coaxial Generator. As the high explosive (HE) detonates from input to output (left to right), the armature is fused to the stator, cutting off the input and forcing the flux into an output coil (not pictured) connecting the armature and the stator. Image from [14].

requiring the magnetic field and current to increase.

This generator is extremely rugged and conserves flux well, though its low impedance limits the load impedance (which itself must to be much less than the generator impedance). Currents in excess of 50 MA have been observed with this generator. It is often used as an extension of the helical generator, which will be mentioned later.

2.7 Disk Generator

Rotating Figure 2-6 around the axis shown on the left yields the disk generator, which is modularly comprised of some number of segments (two of which are shown). In the figure, the x's represent magnetic fields going into the paper and the cross-hatched areas are filled with explosives. The input is at the top of the figure and the load is the loop in the bottom right. Each segment is detonated in series, beginning with the segment closest to the input. When the first segment detonates, it seals off the input and collapses the cavity connecting to the input, forcing the flux into the other cavities. Then the next cavity is collapsed by the next explosion and so on until all of the flux has been forced into the load. If not properly designed and timed, flux can

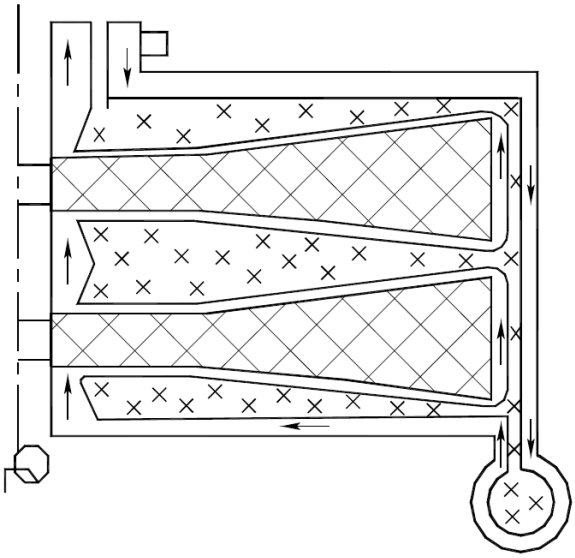

Figure 2-6: Disk Generator. High explosives (represented by the cross-hatched regions) are sequentially detonated to seal off the input (pictured top) and force flux out of the cavities and into the output coil (pictured bottom). Image from [1].

become trapped in isolated cavities, rather than funneled into the load, decreasing efficiency. Flux-trapping in isolated cavities such as improperly collapsed cavities of this generator or pockets formed while metal scrapes across metal in other generators is the primary source of inefficiency in FCGs. Still, this generator has seen currents in excess of 250 MA.

2.8 Helical Generator

The final generator is the most common, saved for last for that reason and because it operates by decreasing inductance in a slightly different manner. Rather than decreasing the area between the armature and the stator, the helical generator decreases the number of turns in the inductor. Recall that turns in an inductor effectively increase the area the magnetic field pierces by a factor of the number of turns, thus increasing the inductance by a square of that factor (for a fixed length, or linearly with the number of turns for a fixed turn density). When the explosive is detonated (once again in a sweeping manner from input to output), the amature shorts with the turns in the inductor, isolating the input. As the explosive wave moves toward

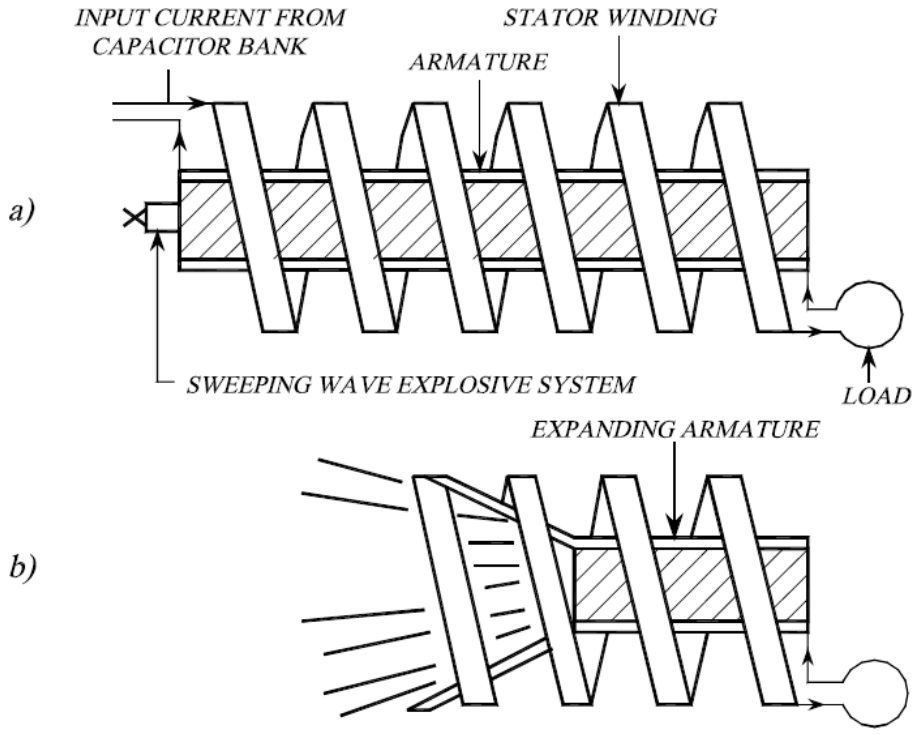

Figure 2-7: Helical Generator, before detonation (a) and mid-explosion (b). Upon detonation, the armature contacts the stator, disconnecting the input. As the explosion progresses, the number of turns decreases, forcing the flux into the output (or load) coil. Image from [1].

the ouput, the turns of the inductor are destroyed, decreasing the inductance and increasing the current and magnetic field amplitude. This generator is often used as a booster, feeding into other generators (such as the coaxial). Similar to the strip generator, the helical generator is of the flimsier variety, being limited by magnetic forces. Currents in helical generators have exceeded 25 MA and their popularity is due in part to high current and energy gains as well as the simplicity of the explosive detonation system.

While much of the literature focuses on larger generators, helical generators have been made as small as 1150 cm^3 [9] and even 100 cm^3 [8].

2.9 Choice of the Loop Generator

Chapter 5 of this thesis presents the design of a loop generator and an experiment to test it. The loop generator was chosen for its robust nature and small form-factor, as required by Draper. These features of the loop generator lend themselves to recent pushes toward both miniaturization and portability. Another contender was the helical generator, as there is far more literature and examples of its miniaturizion, but this generator is of significantly flimsier construction, which is a liability in deployment. Meanwhile, this author expects a loop generator to provide a small and sturdy source in cases where high gain is not necessary. Additionally, should higher gain be required, a series cascade of loop generators can be employed. Finally, the simple construction of the loop generator lends itself to redesign as an example of a gas-expansion powered FCG in Chapter 6.

Chapter 3

Field-Based Model of Flux Compression Generators

FCGs provide both current gain and magnetic field intensity gain, and are often used in pulsed power applications. For this reason, a common means of modeling the dynamics of an FCG is to construct an equivalent circuit [1], [8], [9], [16]. In contrast, this thesis develops an average-field-based model of FCG dynamics. In addition to more directly calculating the fields, this approach more thoroughly treats flux losses to magnetic diffusion in the conductor, which is at times approximated simply as a skin depth that decreases linearly with time [8]. This increased focus on magnetic diffusion becomes an asset in applying the model to lower speed experiments, when flux losses become significant compared to flux compression. We will also see that fields in the near-field, but still far enough away that the device looks like a magnetic dipole, are determined not by internal field strength, but by internal flux, so the model developed here allows for more direct calculation of those fields.

Additionally, the fields-based focus also provides for simple extensibility with magnetic pressure. Rather than prescribing the dynamics of the device by estimating or ignoring the effects of magnetic pressure before calculating the fields, the motion and field intensity can be easily linked, as the field values used for calculating magnetic pressure are the same as for diffusion.

Should the current still be desired, it can be calculated from the inductance (see

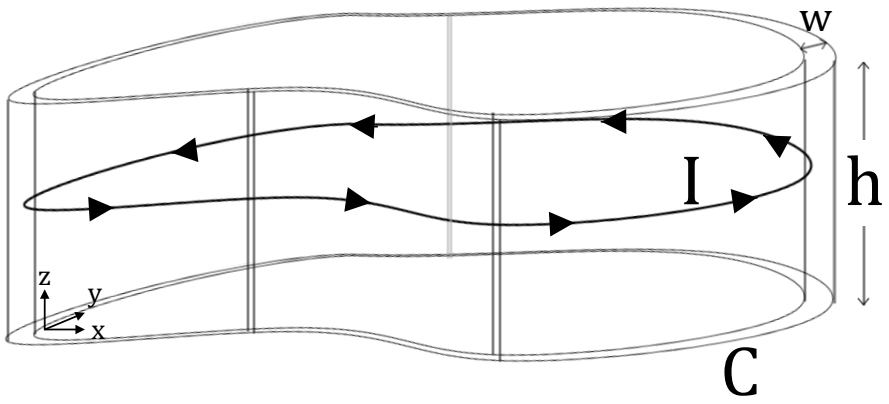

Figure 3-1: Geometry of the FCG. The base of the FCG considered here is represented by the area (lying in the x-y plane) bounded on the outside by a planar curve C and extending in from C by a length w. The FCG is represented by an extrusion of this base for a distance h in the $\hat{\mathbf{z}}$ direction. A current runs around the device parallel to the x-y plane.

the Appendix for discussion of inductance calculations in these devices) paired with the flux in the cavity.

3.1 Geometric Setup

The geometry of the FCG we consider here is given in Figure A-1. The base of the FCG is represented by the area (lying in the x-y plane) bounded on the outside by a planar curve C and extending in from C by a length w. The FCG is represented by an extrusion of this base for a distance h in the $\hat{\mathbf{z}}$ direction. A current runs around the device parallel to the x-y plane, inducing a magnetic field within the cavity, primarily in the $\hat{\mathbf{z}}$ direction.

By varying our choice of C, this geometry can represent the plate generator, the cylindrical implosion generator, the loop generator, and the strip generator from Chapter 2.

To simplify analysis, we will assume a tall device, i.e., h is much larger than the length scale of C and $h \gg w$. (Note that, despite this assumption, the figure shows a short device, where h is on the same order as the length scale as C, even slightly smaller.) With this assumption, the magnetic field within the cavity is approximately

uniform, with negligible $\hat{\mathbf{x}}$ and $\hat{\mathbf{y}}$ components. There is negligible magnetic field outside the device and the field within the conductor is given by the solution to a diffusion equation, since we assume the FCG is constructed from a conductor with conductivity σ.

If our FCG were superconducting, there would be no losses to magnetic diffusion, flux would be perfectly conserved, and the flux in our device would be given exactly by

$$\Lambda_0 = B(t)A(t), \tag{3.1}$$

where Λ_0 is the initial flux, $A(t)$ is the time-varying area of the FCG cavity, and $B(t)$ is the magnetic field in the cavity. Since our FCG is not superconducting, some of the flux is in the conductor rather than the cavity, so

$$\lambda_{total}(t) = B(t)A(t) + \lambda_{cond}(t), \tag{3.2}$$

where $\lambda_{total}(t)$ is the total flux in the device and $\lambda_{cond}(t)$ is the flux lost from the cavity to the conductor by diffusion. Flux in the conductor can be adjacent to the cavity or disconnected; we will first consider as if all flux in the conductor is adjacent to cavity (as in the cylindrical implosion generator), then demonstrate the correction for considering flux losses to conductor isolated from the cavity (as in the loop generator). Note also that the total flux in the device is a function of time. In particular, we expect it to decay as energy stored in the magnetic fields is dissipated in the conductor and converted to heat. In the next section, we develop an expression for $\lambda_{cond}(t)$, after which we will develop an expression for $\lambda_{total}(t)$ and form a system of differential-algebraic-equations.

3.2 Magnetic Diffusion

We now consider the magnetic diffusion problem that arises in solving for the field within the conductor, as pictured in Figure 3-2a.

To simplify analysis and avoid the complexities inherent in an arbitrary curve

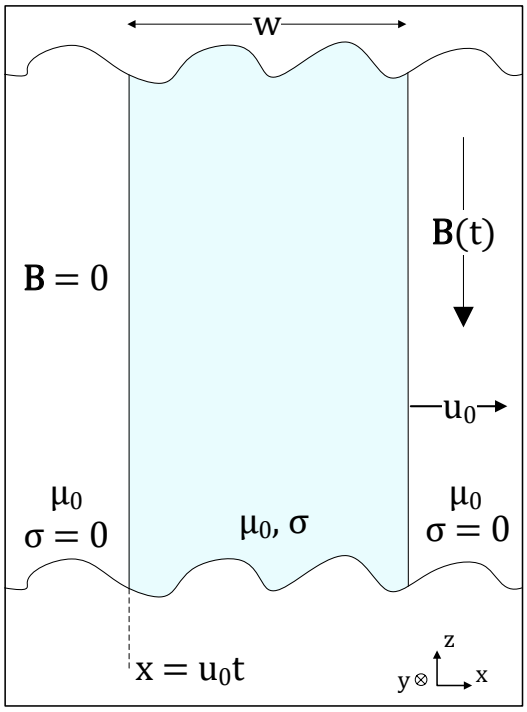

(a) The plate moves with velocity $\mathbf{u} = u_0\hat{\mathbf{x}}$.

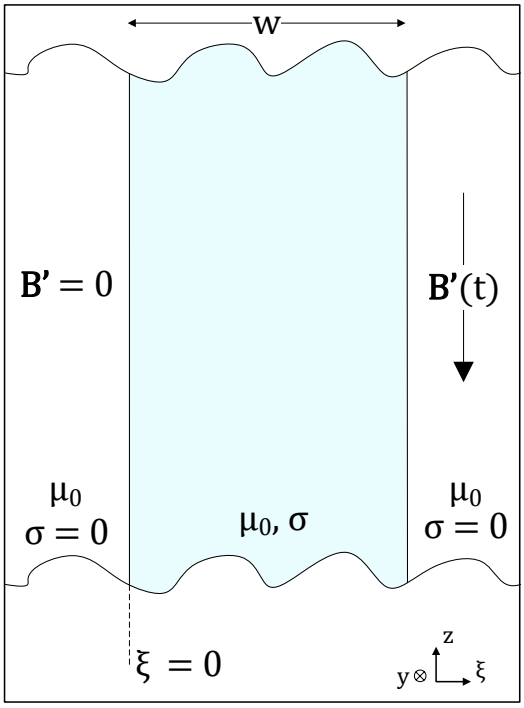

(b) The plate is stationary, with the edge with no magnetic field at $\xi = 0$.

Figure 3-2: Diffusion problem setup. A plate of conductivity σ, permeability μ_0, and constant width w is infinitely tall and infinitely long into the page. On one side the magnetic field is 0 and on the other it is given by $\mathbf{B}(t) = -B_0(t)\hat{\mathbf{z}}$.

C, we first examine the case of a temporally-varying magnetic field diffusing into an infinite plate conductor, with finite but constant width w and conductivity σ. Close to the surface of the conductor, any actual curvature is negligible, thus our use of an approximation as an infinite plate in order to calculate the fields within the conductor. To capture the effect of motion in our device, the plate moves with velocity $u_0\hat{\mathbf{x}}$. (Note that $\hat{\mathbf{x}}$ and $\hat{\mathbf{y}}$ in Figure 3-2 do not necessarily correspond to $\hat{\mathbf{x}}$ and $\hat{\mathbf{y}}$ in Figure A-1.) In a tall device, the magnetic field will be negligible outside the device and nonzero within, so our boundary conditions are given by $\mathbf{B}(x < u_0 t) = 0$ and $\mathbf{B}(x > u_0 t + w) = -B_0(t)\hat{\mathbf{z}}$, where $B_0(t)$ is magnitude of the field on the inside edge of the device. We assume that motion starts at time $t = 0$ and that prior to that, the system had reached steady-state with constant B_0, so the magnetic field inside the conductor was given by $\mathbf{B}(0 < x < w, t \leq 0) = -\frac{x}{w}B_0(0)\hat{\mathbf{z}}$, which corresponds to a uniform current density of $\mathbf{J}(0 < x < w, t \leq 0) = \frac{B_0(0)}{w\mu_0}\hat{\mathbf{y}}$. We can also use the formula here developed to calculate the flux losses, starting at zero flux, from the seed current pulse by prescribing the field ($B = iL_0/A_0$) for the duration of the pulse, then switching to solving the differential equations derived in the following sections. (The current from a capacitor bank seed source may be predicted by a circuit simulation.)

First, we transform into the frame of reference of the plate, using the transformation $\xi = x - u_0 t$. The effects of this transformation on the electric and magnetic fields is given in Section 6.1.1 of [17]. Assuming magnetoquasistatics, the magnetic field and field equations are unchanged by this transformation, so the problem is now set up as in Figure 3-2b. (Note that the field in the reference frame of the plate is $\mathbf{B}'$.) Inside the conductor, the field obeys the following diffusion equation, derived from Maxwell's equations,

$$\frac{\partial \mathbf{B}'}{\partial t} = \frac{1}{\mu_0 \sigma}\nabla'^2 \mathbf{B}', \tag{3.3}$$

which can be simplified to

$$\frac{\partial B'_z}{\partial t} = \frac{1}{\mu_0 \sigma}\frac{\partial^2 B'_z}{\partial \xi^2}, \tag{3.4}$$

since the field inside the conductor is directed in the $-\hat{\mathbf{z}}$ direction and is independent

of y and z. So, we now have to solve the following boundary value problem:

$$\frac{\partial B_z'}{\partial t} = \frac{1}{\mu_0 \sigma} \frac{\partial^2 B_z'}{\partial \xi^2}, 0 < \xi < w; \tag{3.5}$$

$$B_z'(\xi = 0, t) = 0, t \geq 0; \tag{3.6}$$

$$B_z'(\xi = w, t) = -B_0(t), t \geq 0; \tag{3.7}$$

$$B_z'(\xi, t = 0) = -\frac{\xi}{w} B_0(0), 0 \leq \xi \leq w. \tag{3.8}$$

Following the solution in [18], let $u(\xi, t) = -\frac{\xi}{w} B_0(t)$ and $v(\xi, t) = B_z'(\xi, t) - u(\xi, t)$. Then, $\frac{\partial u}{\partial t} + \frac{\partial v}{\partial t} = \frac{1}{\mu_0 \sigma}(\frac{\partial^2 u}{\partial \xi^2} + \frac{\partial^2 v}{\partial \xi^2})$. But, since $\frac{\partial^2 u}{\partial \xi^2} = 0$,

$$\frac{\partial u}{\partial t} + \frac{\partial v}{\partial t} = \frac{1}{\mu_0 \sigma} \frac{\partial^2 v}{\partial \xi^2}. \tag{3.9}$$

The boundary value problem in terms of v is then

$$\left(\frac{\partial}{\partial t} - \frac{1}{\mu_0 \sigma} \frac{\partial^2}{\partial \xi^2} \right) [v] = \frac{\xi}{w} \dot{B}_0(t), 0 < \xi < w; \tag{3.10}$$

$$v(\xi = 0, t) = 0, \tag{3.11}$$

$$v(\xi = w, t) = 0, \tag{3.12}$$

$$v(\xi, t = 0) = 0, 0 < \xi < w. \tag{3.13}$$

The eigenfunctions and eigenvalues associated with this problem are

$$\Xi_n(\xi) = \sin(k_n \xi), k_n = \frac{n\pi}{w}, n \in \mathbb{Z}^+. \tag{3.14}$$

Let $S(\xi,t) = \frac{\xi}{w}\dot{B}_0(t) = \sum_{n=1}^{\infty} \hat{S}_n(t)\sin(k_n\xi)$. Then,

$$\dot{B}_0(t)\int_0^w \frac{\xi}{w}\sin\left(\frac{m\pi\xi}{w}\right)d\xi = \sum_{n=1}^{\infty}\hat{S}_n(t)\int_0^w \xi\sin\left(\frac{m\pi\xi}{w}\right)\sin\left(\frac{n\pi\xi}{w}\right)d\xi; \tag{3.15}$$

$$\dot{B}_0(t)\frac{w}{(m\pi)^2}\int_0^{m\pi} y\sin(y)dy = \sum_{n=1}^{\infty}\hat{S}_n(t)\frac{1}{2}\int_0^w \xi\left(\cos\left(\frac{\pi}{w}(m-n)\xi\right) - \cos\left(\frac{\pi}{w}(m+n)\xi\right)\right)d\xi; \tag{3.16}$$

$$\dot{B}_0(t)\frac{w}{(m\pi)^2}(-m\pi(-1)^m) = \hat{S}_m(t)\frac{w}{2}, \tag{3.17}$$

so

$$\hat{S}_m(t) = \frac{2}{m\pi}(-1)^{m+1}\dot{B}_0(t). \tag{3.18}$$

We also have $v(\xi,t) = \sum_{n=1}^{\infty}\hat{v}_n(t)\sin(k_n\xi)$, so

$$\sum_{n=1}^{\infty}\left(\dot{\hat{v}}_n(t) + \frac{1}{\mu_0\sigma}k_n^2\hat{v}_n(t) - \hat{S}_n(t)\right)\sin(k_n\xi) = 0, \tag{3.19}$$

for all $0 < \xi < w$. For this equality to be true, it must be that

$$\dot{\hat{v}}_n(t) + \frac{n^2\pi^2}{\mu_0\sigma w^2}\hat{v}_n(t) = \hat{S}_n(t), \tag{3.20}$$

for all $n \in \mathbb{Z}^+$. We also have $\hat{v}_n(0) = 0$, since $v(\xi, t=0) = 0$ for all ξ in the interval.

The solution to this first order, linear ODE is

$$\hat{v}_n(t) = \int_0^t e^{-\frac{n^2\pi^2}{\mu_0\sigma w^2}(t-\tau)}\cdot\frac{2}{n\pi}(-1)^{n+1}\dot{B}_0(\tau)d\tau. \tag{3.21}$$

So, the field in the conductor is given by

$$B_z'(\xi,t) = -\frac{\xi}{w}B_0(t) + \frac{2}{\pi}\sum_{n=1}^{\infty}\left(\frac{(-1)^{n+1}}{n}\int_0^t e^{-\frac{n^2\pi^2}{\mu_0\sigma w^2}(t-\tau)}\dot{B}_0(\tau)d\tau\sin\left(\frac{n\pi\xi}{w}\right)\right). \tag{3.22}$$

Transforming back to the stationary frame leaves the magnetic field unchanged, such

that

$$B_z(x,t) = -\frac{x-u_0t}{w}B_0(t) + \frac{2}{\pi}\sum_{n=1}^{\infty} \left(\frac{(-1)^{n+1}}{n}\int_0^t e^{-\frac{n^2\pi^2}{\mu_0\sigma w^2}(t-\tau)}\dot{B}_0(\tau)d\tau \sin\left(\frac{n\pi(x-u_0t)}{w}\right)\right). \quad (3.23)$$

3.3 Flux Loss Dynamics

Now that we have an expression for the field within the conductor, we can calculate the flux lost to the conductor at any moment.

Recall, flux is defined by

$$\lambda(t) = \iint_S \mathbf{B}\cdot d\mathbf{a}. \quad (3.24)$$

In this case, the surface, S, wraps around the perimeter of the cavity with width w and normal vector in the $-\hat{\mathbf{z}}$ direction. So, the flux lost to the conductor is given by

$$\lambda_{cond}(t) = -p(t)\int_{u_0t}^{u_0t+w} B_z(x,t)dx, \quad (3.25)$$

where the perimeter, $p(t)$, is time-varying in general. Thus,

$$\begin{aligned}
\lambda_{cond}(t) =& p(t)\int_{u_0t}^{u_0t+w}\frac{x-u_0t}{w}B_0(t) - \frac{2}{\pi}\sum_{n=1}^{\infty}\left(\frac{(-1)^{n+1}}{n}\int_0^t e^{-\frac{n^2\pi^2}{\mu_0\sigma w^2}(t-\tau)}\dot{B}_0(\tau)d\tau \right.\\
&\left.\sin\left(\frac{n\pi(x-u_0t)}{w}\right)\right)dx \quad (3.26)\\
=& \frac{1}{2}p(t)wB_0(t) - p(t)\frac{2}{\pi}\sum_{n=1}^{\infty}\left(\frac{(-1)^{n+1}}{n}\int_0^t e^{-\frac{n^2\pi^2}{\mu_0\sigma w^2}(t-\tau)}\dot{B}_0(\tau)d\tau \right.\\
&\left.\int_{u_0t}^{u_0t+w}\sin\left(\frac{n\pi(x-u_0t)}{w}\right)dx\right) \quad (3.27)\\
=& \frac{1}{2}p(t)w\left(B_0(t) - \frac{8}{\pi^2}\sum_{n=0}^{\infty}\left(\frac{1}{(2n+1)^2}\int_0^t e^{-\frac{(2n+1)^2\pi^2}{\mu_0\sigma w^2}(t-\tau)}\dot{B}_0(\tau)d\tau\right)\right) \quad (3.28)\\
\approx& \frac{1}{2}p(t)w\left(B_0(t) - \frac{8}{\pi^2}\int_0^t e^{-\frac{\pi^2}{\mu_0\sigma w^2}(t-\tau)}\dot{B}_0(\tau)d\tau\right). \quad (3.29)
\end{aligned}$$

As long as $B_0(t)$ is increasing ($\dot{B}_0(t) \geq 0$), which is expected of flux compression,

truncation of the series overestimates the flux losses to the conductor, since every term dropped from the summation was being subtracted from the first order guess of $p(t)wB_0(t)/2$ (which would be the flux if the field dropped off linearly in x over the whole width from $B_0(t)$ at $u_0t + w$ to 0 at u_0t).

In order reformulate this equation for easier solution, we differentiate it, truncate the series, and substitute,

$$\dot{\lambda}_{cond}(t) = \frac{d}{dt}\left[\frac{1}{2}p(t)w\left(B_0(t) - \frac{8}{\pi^2}\sum_{n=0}^{\infty}\left(\frac{1}{(2n+1)^2}\int_0^t e^{-\frac{(2n+1)^2\pi^2}{\mu_0\sigma w^2}(t-\tau)}\dot{B}_0(\tau)d\tau\right)\right)\right] \tag{3.30}$$

$$= \frac{\dot{p}}{p}\lambda_{cond} + \frac{1}{2}pw\left(\dot{B}_0(t) - \frac{8}{\pi^2}\sum_{n=0}^{\infty}\frac{1}{(2n+1)^2}\left(\dot{B}_0(t) - \frac{(2n+1)^2\pi^2}{\mu_0\sigma w^2}\int_0^t e^{-\frac{(2n+1)^2\pi^2}{\mu_0\sigma w^2}(t-\tau)}\dot{B}_0(\tau)d\tau\right)\right) \tag{3.31}$$

$$= \frac{\dot{p}}{p}\lambda_{cond} + \frac{4}{\mu_0\sigma w}p(t)\sum_{n=0}^{\infty}\int_0^t e^{-\frac{(2n+1)^2\pi^2}{\mu_0\sigma w^2}(t-\tau)}\dot{B}_0(\tau)d\tau \tag{3.32}$$

$$\approx \frac{\dot{p}}{p}\lambda_{cond} + \frac{4}{\mu_0\sigma w}p(t)\int_0^t e^{-\frac{\pi^2}{\mu_0\sigma w^2}(t-\tau)}\dot{B}_0(\tau)d\tau \tag{3.33}$$

$$\approx \frac{\dot{p}}{p}\lambda_{cond} + \frac{4}{\mu_0\sigma w}\left(\frac{\pi^2}{4w}\right)\left(\frac{1}{2}p(t)wB_0(t) - \lambda_{cond}\right) \tag{3.34}$$

$$= \frac{\pi^2 p(t)}{2\mu_0\sigma w}B_0(t) + \left(\frac{\dot{p}}{p} - \frac{\pi^2}{\mu_0\sigma w^2}\right)\lambda_{cond}. \tag{3.35}$$

Here we have truncated the series once more, which now underestimates the growth of flux losses in the conductor.

3.4 Total System Flux Evolution

Having calculated the relation between the flux in the conductor and the field strength in the cavity, we now consider the evolution of total flux in the device. In the perfectly conducting case, the total flux is constant and in the mechanically static case, we would expect exponential decay of the flux, as in an LR circuit. To quantify the decay in general, we first apply Leibniz integral rule to differentiate the total flux

from the magnetic field not only in the cavity, but also the conductor (which pierces a moving surface S', bounded by C' on the outer edge of the device),

$$\dot{\lambda}_{total} = \frac{d}{dt} \iint_{S'(t)} \mathbf{B} \cdot d\mathbf{a} \tag{3.36}$$

$$= \iint_{S'(t)} \left(\frac{\partial \mathbf{B}}{\partial t} + (\nabla \cdot \mathbf{B})\mathbf{u} \right) \cdot d\mathbf{a} - \oint_{C'(t)} \mathbf{u} \times \mathbf{B} \cdot d\mathbf{s}, \tag{3.37}$$

where $\mathbf{u}$ is the velocity of the surface/boundary element. Applying Gauss's law for magnetism ($\nabla \cdot \mathbf{B} = 0$) and Faraday's law of induction ($\iint_{S'(t)} \frac{\partial \mathbf{B}}{\partial t} \cdot d\mathbf{a} = -\oint_{C'(t)} \mathbf{E} \cdot d\mathbf{s}$, where $\mathbf{E}$ is the electric field),

$$\dot{\lambda}_{total} = -\oint_{C'(t)} (\mathbf{E} + \mathbf{u} \times \mathbf{B}) \cdot d\mathbf{s}. \tag{3.38}$$

Ohm's law relates the current density, $\mathbf{J}$, to the electric and magnetic fields by $\mathbf{J} = \sigma(\mathbf{E} + \mathbf{u} \times \mathbf{B})$). So,

$$\dot{\lambda}_{total} = -\oint_{C'} \frac{\mathbf{J}}{\sigma} \cdot d\mathbf{s}. \tag{3.39}$$

Assuming the conductivity and surface current density are uniform around the device, we have

$$\dot{\lambda}_{total} = -\frac{J(t) p_o(t)}{\sigma}, \tag{3.40}$$

where $p_o(t)$ is the outer perimeter of the generator and J is the magnitude of the current density on the outer edge of the conductor, which can be calculated from the results of our diffusion problem. For simplicity, in the remainder of the chapter we will assume the walls of the device are thin enough that the inner and outer perimeters are equal ($p(t) \approx p_o(t)$), but the analysis could be similarly carried out without this assumption in the case of thick walls.

Quasistatic Ampere's Law states $\nabla \times \mathbf{B} = \mu_0 \mathbf{J}$, which means

$$\dot{\lambda}_{total}(t) = -\frac{p(t)}{\sigma} J_y(x = u_0 t, t) \tag{3.41}$$

$$= \frac{p(t)}{\sigma} \frac{\partial}{\partial x} \left[\frac{B_z}{\mu_0}\right]\Bigg|_{x=u_0 t} \tag{3.42}$$

$$= -\frac{p(t)}{\mu_0 \sigma w} \left(B_0(t) + 2 \sum_{n=1}^{\infty} (-1)^{n+1} \int_0^t e^{-\frac{(n\pi)^2}{\mu_0 \sigma w^2}(t-\tau)} \dot{B}_0(\tau) d\tau \right) \tag{3.43}$$

$$\approx -\frac{p(t)}{\mu_0 \sigma w} \left(B_0(t) + 2 \int_0^t e^{-\frac{\pi^2}{\mu_0 \sigma w^2}(t-\tau)} \dot{B}_0(\tau) d\tau \right) \tag{3.44}$$

$$\approx -\frac{p(t)}{\mu_0 \sigma w} \left(B_0(t) - \frac{\pi^2}{4} \left(\frac{2\lambda_{cond}}{p(t) w} - B_0(t) \right) \right) \tag{3.45}$$

$$= -\frac{p(t)}{\mu_0 \sigma w} \left(1 + \frac{\pi^2}{4}\right) B_0(t) + \frac{\pi^2}{4 \mu_0 \sigma w^2} \lambda_{cond}. \tag{3.46}$$

The alternating series in eq. (3.43) is overestimated by truncation, since it's strictly decreasing when $\dot{B}_0 > 0$, as expected. The substitution of λ_{cond} decreases the overestimation, but does not fully counteract it, so equation eq. (3.46) still overestimates the rate of flux loss.

Collecting eqs. (3.2), (3.35) and (3.46) and replacing the "prescribed" function $B_0(t)$ with the coupled field strength variable, B, we arrive at the following set of differential-algebraic-equations governing the magnetic evolution of the device:

$$\dot{\lambda}_{total} = -\frac{p(t)}{\mu_0 \sigma w} \left(1 + \frac{\pi^2}{4}\right) B + \frac{\pi^2}{4 \mu_0 \sigma w^2} \lambda_{cond}, \tag{3.47}$$

$$\dot{\lambda}_{cond} = \frac{p(t)}{\mu_0 \sigma w} \cdot \frac{\pi^2}{2} B + \left(\frac{\dot{p}}{p} - \frac{\pi^2}{\mu_0 \sigma w^2} \right) \lambda_{cond}, \tag{3.48}$$

$$\lambda_{total} = A(t) B + \lambda_{cond}. \tag{3.49}$$

If neglecting the effects of magnetic pressure, one must prescribe $A(t)$ and $p(t)$. In order to add the effects of magnetic pressure, one would at this point add equations relating the magnetic field value, $B(t)$, to the geometric dynamics given by $A(t)$ and $p(t)$. In the next two sections we will examine the cylindrical implosion generator and the loop generator, accounting for magnetic pressure.

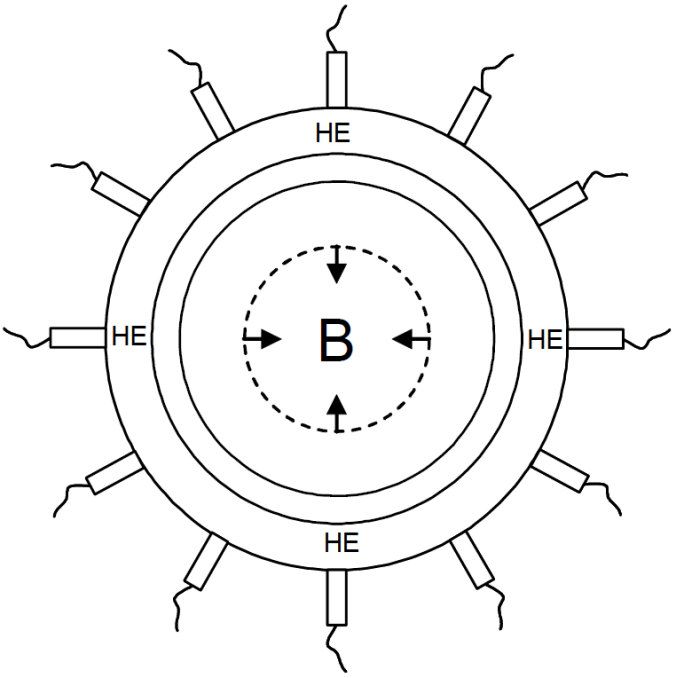

Figure 3-3: Cylindrical Implosion Generator. Simultaneous detonation of the high explosive (HE) decreases the area of the cylinder, compressing the flux and increasing the field strength. Image from [14].

Recall that the total flux in the cavity is given by $i(t)L(t) = B(t)A(t)$, where $i(t)$ is the total current in the device and $L(t)$ is what the inductance would be if the metal were perfectly conducting (all currents run on the inner surface, diffusion can be discounted, so we can only consider the flux in the cavity), so the current can be calculated from this model in postprocessing. Keeping with our assumption of a long device, the inductance is approximately given by $L(t) = \mu_0 A(t)/l$, where l is the height of the device. For a more accurate calculation of the inductance that does not make use of the approximation of a long device, see the Appendix.

3.5 Example: Cylindrical Implosion Generator

In this section, we consider the cylindrical implosion generator and include the effect of magnetic pressure. Since the exact relation between the field (equivalently the magnetic pressure), the perimeter, and the area is entirely geometry dependent, we first consider the simple, but illustrative, example of the cylindrical implosion

generator, then move onto the slightly more complicated loop generator in the next section.

The forces at play in considering the mechanical dynamics of the generator are inertia, elasticity, the force of the explosion, and the pressure from the magnetic field in the cavity. For a higher-fidelity model, all of these can be considered and included in the model, but that goes beyond the scope of this thesis. The force of the explosion is most relevant during the initial acceleration of the liner and can be accounted for by using Gurney analysis to calculate the initial velocity [19]. Derived from conservation of energy, Gurney analysis tells us the approximate velocity of the expanding metal after explosive has fully detonated and accelerated it. Once the cylinder has reached this velocity, the force from the explosion is no longer a consideration and the model presented here assumes that his velocity is reached so quickly as to be considered instantaneous. In this section, the velocity will actually be a tuning parameter to match experimental data, but in the next section the velocity is derived from Gurney analysis, so see there for an example and more information. At high magnetic field strengths, the magnetic pressure exceeds the stress from elastic deformation, so for simplicity this example model will ignore elasticity, though an elasticity term can certainly be added and should yield more accurate predictions.

Conservation of mass demands that as the cylinder implodes either the width or the density of the shell increases. To simplify analysis in section 3.2, it was assumed that the width is constant, so this model necessarily assumes the density increases. (In other geometries, such as the loop considered in the next section, the density is decreasing, since the shell is exploding instead of imploding.) To develop a higher-fidelity model, one would need to solve the diffusion problem with moving boundary conditions and then either prescribe the width or couple the evolution of the width to the system dynamics.

The uniform magnetic field provides a uniform pressure of $B^2/(2\mu_0)$ over the surface of the conductor [11]. Assuming the dominant net force on the conductor is

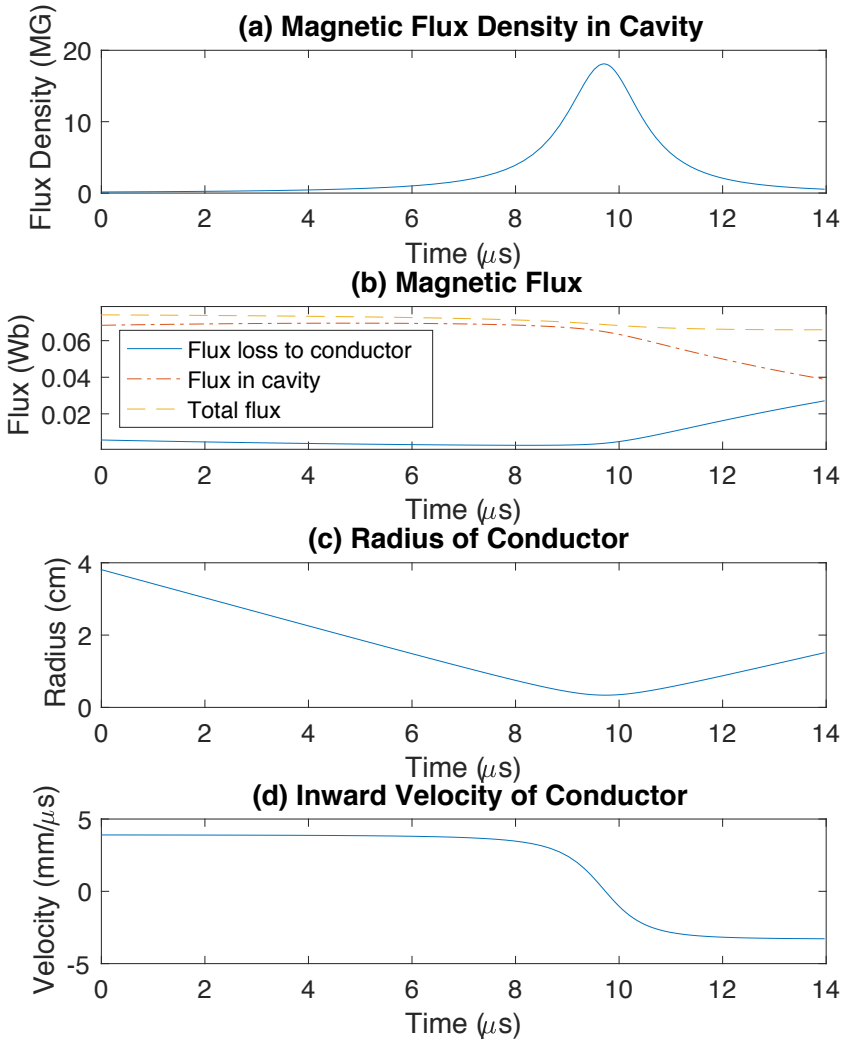

Figure 3-4: Dynamics of a cylindrical implosion FCG. Plot (a) shows the magnetic flux density (B) as a function of time. It reaches a maximum value of 18.1 MG and the pulse has a full width at half max of 1.68 μs. Plot (b) shows the flux in the cavity ($B \cdot A$), in the conductor (λ_{cond}), and in total in the device (λ_{total}) as a function of time. Plot (c) shows the radius of the conducting cylinder (r) as a function of time. It reaches a minimum of 3.38 mm before increasing due to the effects of magnetic pressure within the cavity. Plot (d) shows the inward velocity of the conductor ($v = -\dot{r}$) as a function of time. The parameters used in this simulation are summarized in Table 3.1.

that of the magnetic pressure, Newton's second law gives

$$m\ddot{r} = Area \cdot Pressure = 2\pi rl \cdot \frac{B^2}{2\mu_0}, \tag{3.50}$$

where m is the mass of the conductor (assumed constant), r is the radius, and l is the height. So, accounting for magnetic pressure and diffusion, a long cylindrical implosion generator follows

$$\dot{\lambda}_{total} = -\frac{2\pi}{\mu_0 \sigma w}\left(1 + \frac{\pi^2}{4}\right) rB + \frac{\pi^2}{4\mu_0 \sigma w^2}\lambda_{cond}, \tag{3.51}$$

$$\dot{\lambda}_{cond} = \frac{\pi^3}{\mu_0 \sigma w} rB - \left(\frac{v}{r} + \frac{\pi^2}{\mu_0 \sigma w^2}\right)\lambda_{cond} \tag{3.52}$$

$$\lambda_{total} = \pi r^2 B + \lambda_{cond} \tag{3.53}$$

$$\dot{r} = -v \tag{3.54}$$

$$\dot{v} = -\frac{\pi l}{m}\frac{B^2}{\mu_0} r, \tag{3.55}$$

where the additional state variable, v, represents the inward radial velocity of the conductor.

Table 3.1: Parameters for simulated cylindrical implosion generator

Parameter	Symbol	Value
Initial inner radius	r_0	3 in.
Initial radial velocity	v_0	3 $mm/\mu s$
Wall thickness	w	0.125 in.
Height	l	2 in.
Initial magnetic field in cavity	B_0	15 T
Conductivity	σ	16.52 kS/mm [20]
Magnetic permeability	μ_0	$4\pi \times 10^{-7} H/m$ [17], [20]
Density	ρ_{brass}	$8.73\, g/cm^3$ [20]

Figure 3-4 shows the results of this model applied to a brass cylindrical implosion generator with initial metal velocity of 3 $mm/\mu s$, thickness (w) 1/8 inch, initial radius 3 inches, and initial magnetic field 15 T. The conductivity of brass is assumed to be 16.52 kS/mm and its initial density is assumed to be $8.73\,g/cm^3$ [20]. (Note that since the mass and length only enter in terms of their ratio, one can simply supply the density of the metal and the ratio m/l is this density multiplied by the cross-sectional area, $\pi(2wr + w^2)$.) The relative magnetic permeability of brass is 1.0 [20], so its absolute magnetic permeability is $4\pi \times 10^{-7} H/m$ [17]. These parameters are summarized in Table 3.1. The model predicts that after sufficient magnetic field compression the momentum from the explosion will be dissipated and the cylinder will begin to expand again, a phenomenon known as turnaround, which has been experimentally observed [1]. The model developed here predicts device operation prior to failure, but has no means of predicting the moment of device failure. While turnaround has been observed experimentally, it is short-lived prior to the destruction of the generator, whereas this model will predict behavior long beyond the point of actual failure, acting as if the generator never comes apart.

Figure 3-4b shows the evolution of flux in the generator. As turnaround is reached, the total flux begins to decrease noticeably and the flux in the cavity becomes a smaller proportion of the total flux as the flux lost to the conductor ticks up.

Figure 3-5 compares the results of applying this model to the same generator with the experimental and theoretical results presented in Figure 4 of [21]. Plot (a) is based off an initial metal velocity of 3 $mm/\mu s$ and initial magnetic field of 4 T. The experimental data is from Figure 4 of [21]. The initial velocity used in the proposed model was tuned for agreement with experimental data. Plot (b) is based off an initial metal velocity of 4 $mm/\mu s$ and initial magnetic field of 5 T. The initial velocity used in the proposed model was tuned to align turnaround. Plot (c) is based off an initial metal velocity of 3.9 $mm/\mu s$ and initial magnetic field of 15 T. The data in plots (b) and (c) based off the Hoyt & Kazek model are also from Figure 4 of [21]. The initial velocities used in the proposed model in plots (b) and (c) were tuned to align turnaround. Despite neglecting elasticity, there is good agreement between the

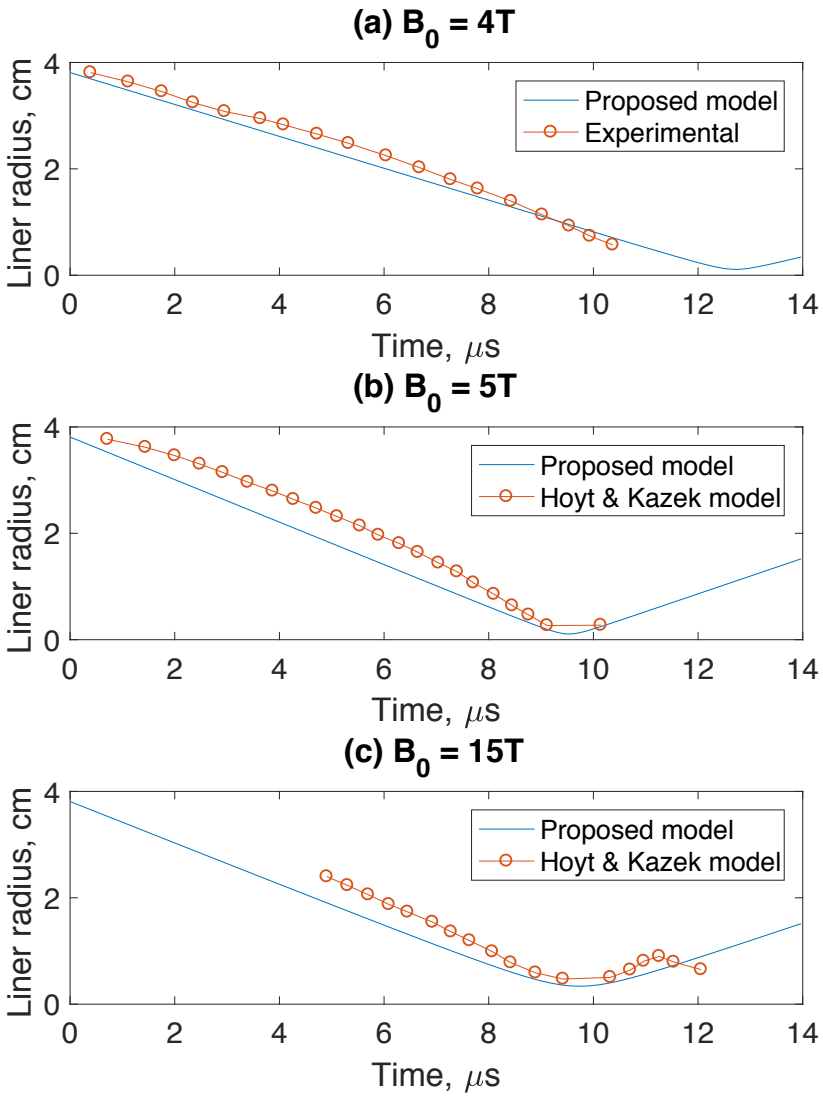

Figure 3-5: Motion of shell in cylindrical implosion generator. With the exception of the initial velocity and initial magnetic field, the resutls of the proposed model are based off the parameters in Table 3.1. The initial velocity used in the proposed model was tuned for agreement with experimental data. The experimental data is from Figure 4 of [21]. The data based off the Hoyt & Kazek model are also from Figure 4 of [21]. Plot (a) is based off an initial metal velocity of 3 $mm/\mu s$ and initial magnetic field of 4 T. Plot (b) is based off an initial metal velocity of 4 $mm/\mu s$ and initial magnetic field of 5 T. Plot (c) is based off an initial metal velocity of 3.9 $mm/\mu s$ and initial magnetic field of 15 T.

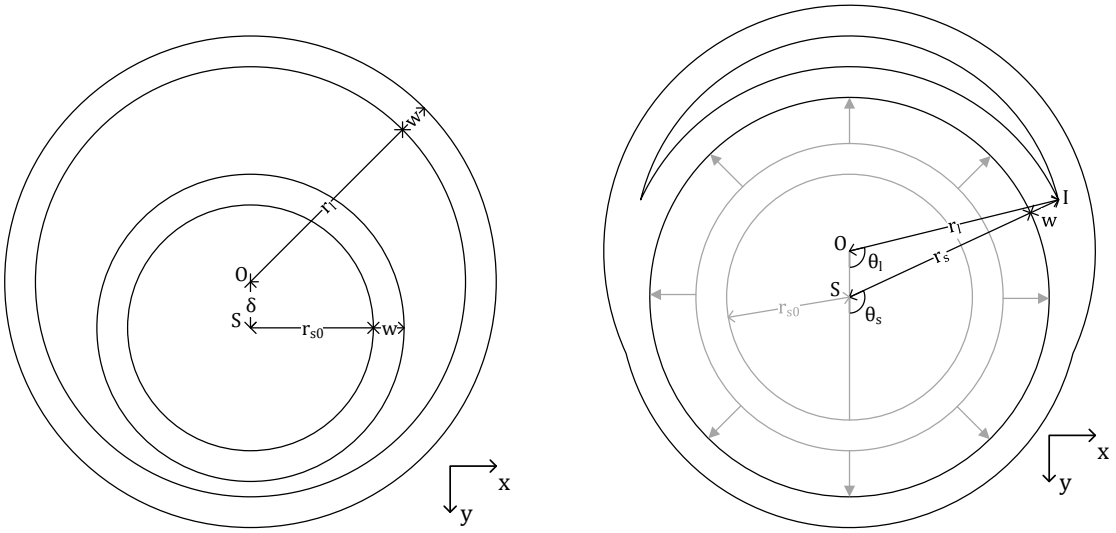

(a) Geometry before detonation.

(b) Geometry during explosion. (The initial position of the shell is also shown in gray.)

Figure 3-6: Geometry of Loop Generator. Detonation of high explosive in the inner shell compresses the area in between the shell and the outer loop. The loop and shell both have width w, i.e., are annular with outer radii exceeding their inner radii by w. The loop has radius r_l and is centered at point O, the origin of the Cartesian system. The shell has initial radius r_{s0} and is centered at point S, displaced $+\delta$ in the y-direction from Point O. It then expands to inner radius r_s, while maintaining width w. Now the shell and loop intersect at two points; the intersection point with positive abscissa is I. The angle $\angle IOS$ has measure θ_l. The angle $\angle ISO$ has measure $\pi - \theta_s$.

experimental/theoretical results of [21] and the results of the model proposed here. Plot (a) highlights the need for a means of predicting device failure, as the proposed mode always predicts turnaround, but in the experiment the device failed first. In all the plots, the proposed model is less concave than the results of [21]. This concavity could be a result of acceleration of the shell by the explosion in finite time, rather than instantaneously as assumed by the proposed model.

3.6 Example: Loop Generator

Having considered the simple case of the cylindrical implosion generator, we consider the loop generator, which is of similar design, but with reverse operation (explosion

rather than implosion). Recall from Chapter 2, that the loop generator (pictured in Figure 3-6) compresses flux by decreasing the area between a static outer loop and an expanding inner shell. The initial flux is assumed to be entirely in the cavity between the loop and the shell, with no flux inside the shell. This flux configuration would be a consequence of a current induced in the shell from the seed-current in the loop.

First we will rewrite the flux accounting equations derived in section 3.4 of this chapter in terms of state variables of this topology, which we choose as the radius of the shell, r_s, and the outward radial velocity of the shell, $v_s = \dot{r}_s$. With the origin of the Cartesian coordinate system at the center of the loop, as in Figure 3-6, any point, (x, y), on the inner surface of the loop will be given by $x^2 + y^2 = r_l^2$, where r_l is the radius of the loop. Since the center of the shell is displaced by a distance δ in the $+\hat{\mathbf{y}}$ direction from the center of the loop and the loop has width w (still assumed constant), any point, (x, y), on the outer surface of the shell is given by $x^2 + (y-\delta)^2 = (r_s + w)^2$. Combining these two equations shows that any intersection point has an ordinate of $y_I = \frac{\delta}{2} + \frac{(r_l - r_s - w)(r_l + r_s + w)}{2\delta}$. Once the shell has expanded to contact the loop ($r_s > r_l - w - \delta$), and until the shell has expanded to fill the loop ($r_s < r_l + \delta - w$), there are two intersection points, each with the same ordinate and opposite abscissa. The angle from the center of the loop to the intersection point is given by $\theta_l = \cos^{-1}\left(\frac{y_I}{r_L}\right)$. The angle from the center of the shell to the intersection point is given by $\theta_s = \cos^{-1}\left(\frac{y_I - \delta}{r_s + w}\right)$. If the shell has not yet contacted the loop, arccosine is not defined, so we define $\theta_l = \theta_s = 0$. If the shell has already filled the loop, arccosine is not defined, so we define $\theta_l = \theta_s = \pi$. Now, the length of the conducting path (the perimeter) is given by $p = 2r_l(\pi - \theta_l) + 2(r_s + w)(\pi - \theta_s)$ and the area of the cavity is given by $A = r_l^2(\pi - \theta_l + \frac{1}{2}\sin(2\theta_l)) - (r_s + w)^2(\pi - \theta_s + \frac{1}{2}\sin(2\theta_s))$. We also require a formula for the derivative of the perimeter, $\dot{p} = -2r_l\dot{\theta}_l - 2(r_s + w)\dot{\theta}_s + 2v_s(\pi - \theta_s)$, where $\dot{\theta}_l = \frac{v_s(r_s+w)}{\delta\sqrt{r_l^2 - y_I^2}}$ and $\dot{\theta}_s = \frac{v_s((r_s+w)^2 + \delta(y_I - \delta))}{\delta(r_s+w)\sqrt{(r_s+w)^2 - (y_I - \delta)^2}}$. To add the effects of a load loop (as shown in Figure 2-3), simply add the constant area and perimeter of the load loop to the variable area and perimeter between the shell and the loop.

An important difference between the cylindrical implosion generator and the loop generator now becomes relevant. Changes in the perimeter in the cylindrical implosion

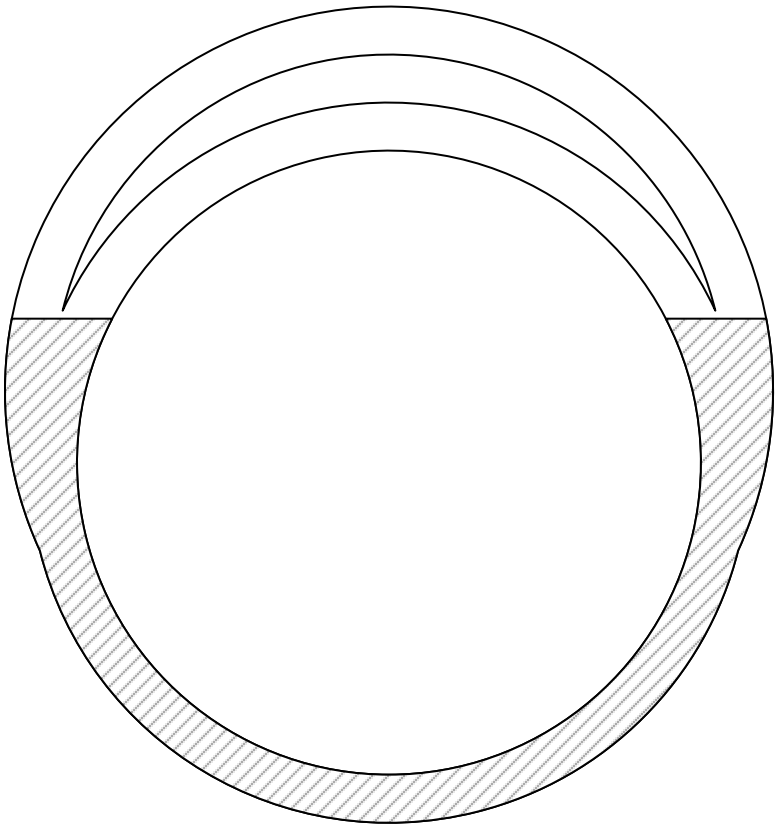

Figure 3-7: Flux reservoir disconnected from conducting path. The shaded area represents a third reservoir for flux, the first two being the cavity and the conductor adjacent to the cavity. Flux in the third reservoir is left behind from motion of the shell along the loop, unlike the flux in conducting path, which comes from diffusion.

generator were only due to deformations of the conducting path, whereas changes in the perimeter of the loop generator come both from expansion of the shell and the shell sliding along the loop; in fact, the dominant factor is the shell sliding along the loop, as the perimeter ultimately decreases after contact between the shell and loop, which is designed to occur early on. This difference means that we must consider a third reservoir for the flux (depicted in Figure 3-7 by the shaded area), the first two being the cavity and the conductor adjacent to the cavity. The magnetic field within the cavity diffuses into the conductor adjacent to the cavity according to eq. (3.35). The shaded area in Figure 3-7, however, is not adjacent to the cavity and so does not obey eq. (3.35). Instead, the flux in this new reservoir is the flux that remains in the edges of the loop and shell that collide to form this area.

Now we have $\lambda_{total} = BA + \lambda_{cond} + \lambda_{lost}$, where λ_{lost} is the flux lost to the new flux reservoir. The differential equation for the evolution of λ_{lost} is simple due to our assumption that flux in the conducting path is uniformly distributed around the perimeter. We can assume that the flux lost to the conductor in this manner is this flux density times the portion of the rate of change of the perimeter from loss of the conducting path, i.e., $\dot{\lambda}_{lost} = \left(2r_l\dot{\theta}_l + 2(r_s + w)\dot{\theta}_s\right)\frac{\lambda_{cond}}{p}$. Note that this corresponds to and is opposite to that portion of the $\frac{\dot{p}}{p}\lambda_{cond}$ term in eq. (3.35), which already accounts for the loss of this flux from the conductor adjacent to the cavity. We also could have developed this more generally in the previous section by splitting the rate of change of the perimeter into its two components: stretching and sliding. The flux accounting equations, updated with this new type of flux, is

$$\dot{\lambda}_{total} = -\frac{p}{\mu_0\sigma w}\left(1 + \frac{\pi^2}{4}\right)B + \frac{\pi^2}{4\mu_0\sigma w^2}\lambda_{cond}, \tag{3.56}$$

$$\dot{\lambda}_{cond} = \frac{p}{\mu_0\sigma w}\cdot\frac{\pi^2}{2}B + \left(\frac{\dot{p}}{p} - \frac{\pi^2}{\mu_0\sigma w^2}\right)\lambda_{cond}, \tag{3.57}$$

$$\lambda_{total} = AB + \lambda_{cond} + \lambda_{lost}. \tag{3.58}$$

$$\dot{\lambda}_{lost} = \left(2r_l\dot{\theta}_l + 2(r_s + w)\dot{\theta}_s\right)\frac{\lambda_{cond}}{p} \tag{3.59}$$

Substituting the above geometric definitions into these equations gives four

differential-algebraic equations in six variables (λ_{total}, λ_{cond}, λ_{lost}, B, r_s, and v_s). One of the remaining differential equations is the definition of the radial velocity:

$$v_s = \dot{r}_s. \tag{3.60}$$

The final differential equation comes from Newton's Second Law applied to the pressure on the shell.

We will once again assume that the pressure is uniform over the conducting surface, however since the loop is fixed in place, the shell alone responds mechanically to the force of the pressure on its surface alone. In keeping with the assumptions put forward earlier in this section about the evolution of the shape of the generator, the pressure of $B^2/(2\mu_0)$ is only felt on an area of $2(\pi - \theta_s)r_s l$, which itself only has a mass of $m \cdot (\pi - \theta_s)/\pi$, where m is the original mass of the entire shell, since now only a sector of angle $2(\pi - \theta_s)$ is experiencing the pressure. Newton's Second Law yields the final differential equation, $(\pi - \theta_s)/\pi \cdot m\dot{v}_s = -2(\pi - \theta_s)r_s l \cdot B^2/(2\mu_0)$, or

$$\dot{v}_s = -\frac{\pi l}{m}\frac{B^2}{\mu_0}r_s. \tag{3.61}$$

Table 3.2: Design parameters for loop generator

Parameter	Symbol	Value
Loop inner radius	r_l	1.75 in.
Shell inner radius	r_{s0}	1 in.
Loop and shell wall thickness	w	0.25 in.
Loop and shell center displacement	δ	0.375 in.
Height	l	2 in.
Initial magnetic field in cavity	B_0	0.375 in.
Copper Conductivity	σ	58.5 kS/mm [22]
Copper Magnetic permeability	μ_0	$4\pi \times 10^{-7} H/m$ [17], [22]

Parameter	Symbol	Value
Copper Density	ρ_{Cu}	$8.93\,g/cm^3$ [22]
C-4 Density	ρ_{C4}	$1.59\,g/cm^3$ [23]
C-4 Gurney velocity	$\sqrt{2E}$	2.176 km/s [24]

Figure 3-8 shows the results of simulating a copper loop generator with loop inner diameter 3.5 inches, shell initial inner diameter 2 inches (both with thickness 1/4 inch), height 2 in., and separation $\delta = 3/8$ inch. The conductivity of copper is assumed to be 58.5 kS/mm and its initial density is assumed to be $8.93\,g/cm^3$ [22]. (Once again, the mass and length only enter the equations as a ratio, so the density is sufficient information.) The magnetic permeability of copper is also $4\pi \times 10^{-7} H/m$ [17]. Here we assume the high explosive is C-4. Filling the shell requires $\pi r_{s0}^2 l \rho_{C4} = 0.16\,kg = 0.36\,lb$ of C-4, where ρ_{C4} is the mass density of C-4, $1.59\,g/cm^3$ [23]. These simulation parameters are summarized in Table 3.2.

To calculate the initial velocity of the shell, we use Gurney analysis [19]. For a cylinder of charge accelerating a metallic lining, this velocity is $v = \sqrt{2E}\left(\frac{M}{C} + \frac{1}{2}\right)^{-1}$, where E is the specific Gurney energy of the explosive and $\sqrt{2E}$ is the Gurney velocity of the explosive (2.176 km/s for C-4 [24]) and M/C is the ratio of the mass of the metal and the mass of the explosive. The shell has a mass of $\pi\left((r_{s0}+w)^2 - r_{s0}^2\right) l \rho_{Cu} = 0.52\,kg$, where ρ_{Cu} is the density of copper, $8.93\,g/cm^3$ [22]. The ratio of the mass of the shell to the mass of the explosives is $\frac{M}{C} = \frac{w(2r_{s0}+w)\rho_{Cu}}{r_{s0}^2 \rho_{C4}} = 3.2$. So, assuming the explosion immediately accelerates the lining, the initial radial velocity of the liner is 1.138 km/s.

The generator in the simulation is unloaded, so device operation ceases upon mechanical failure. Unfortunately, device failure is a highly nonlinear process and difficult to predict, so we make the simple assumption that the device fails at the point that the magnetic pressure within the device exceeds the ultimate tensile strength of copper (455 MPa [22]). With a load, one can stop the simulation after the shell has expanded to fill the loop, which will never happen without a load, as the magnetic

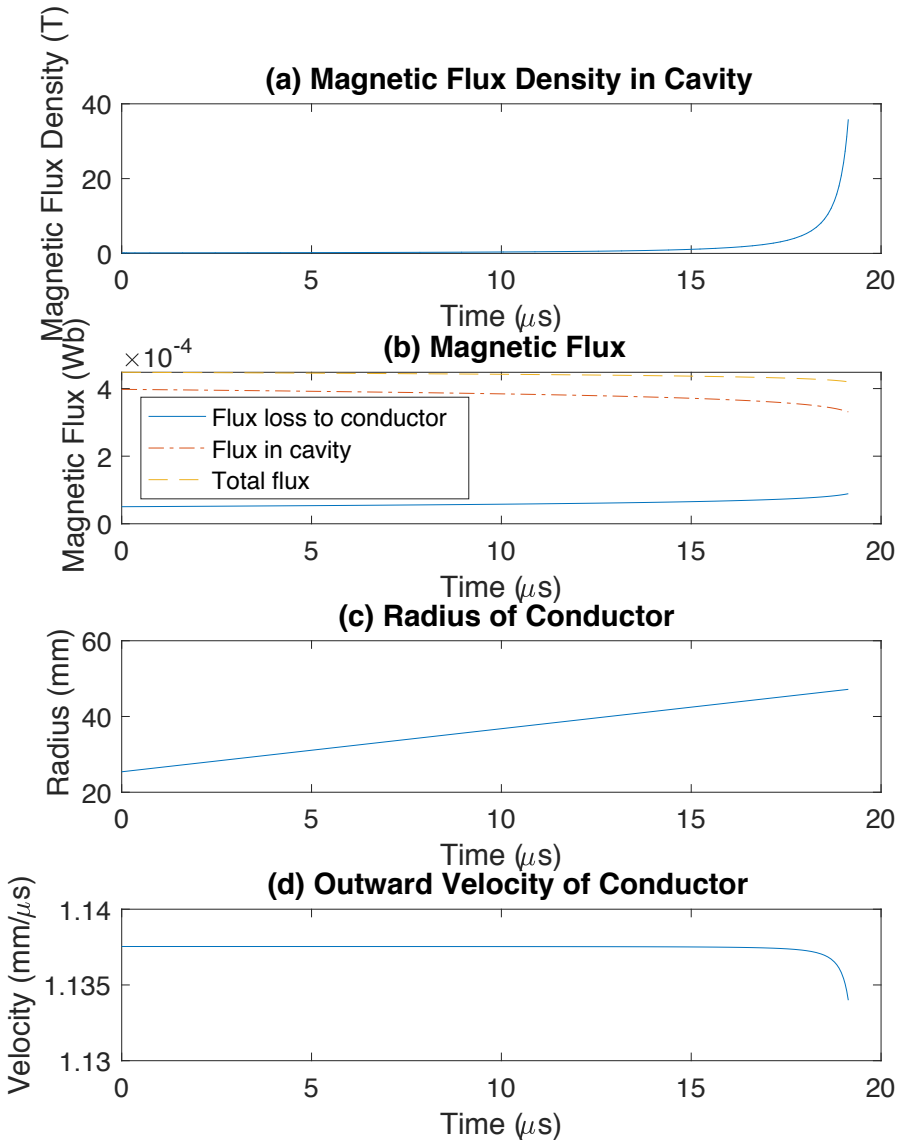

Figure 3-8: Dynamics of an unloaded loop FCG. The parameters used in this simulation are summarized in Table 3.2. Plot (a) shows the magnetic flux density (B) as a function of time. The simulation is ended once the magnetic pressure within the cavity exceeds the ultimate tensile strength of the conductor. Plot (b) shows the flux in the cavity ($B \cdot A$), in the conductor (λ_{cond}), and in total in the device (λ_{total}) as a function of time. Plot (c) shows the radius of the conducting cylinder (r) as a function of time. Plot (d) shows the outward radial velocity of the conducting shell ($v_s = \dot{r}_s$) as a function of time.

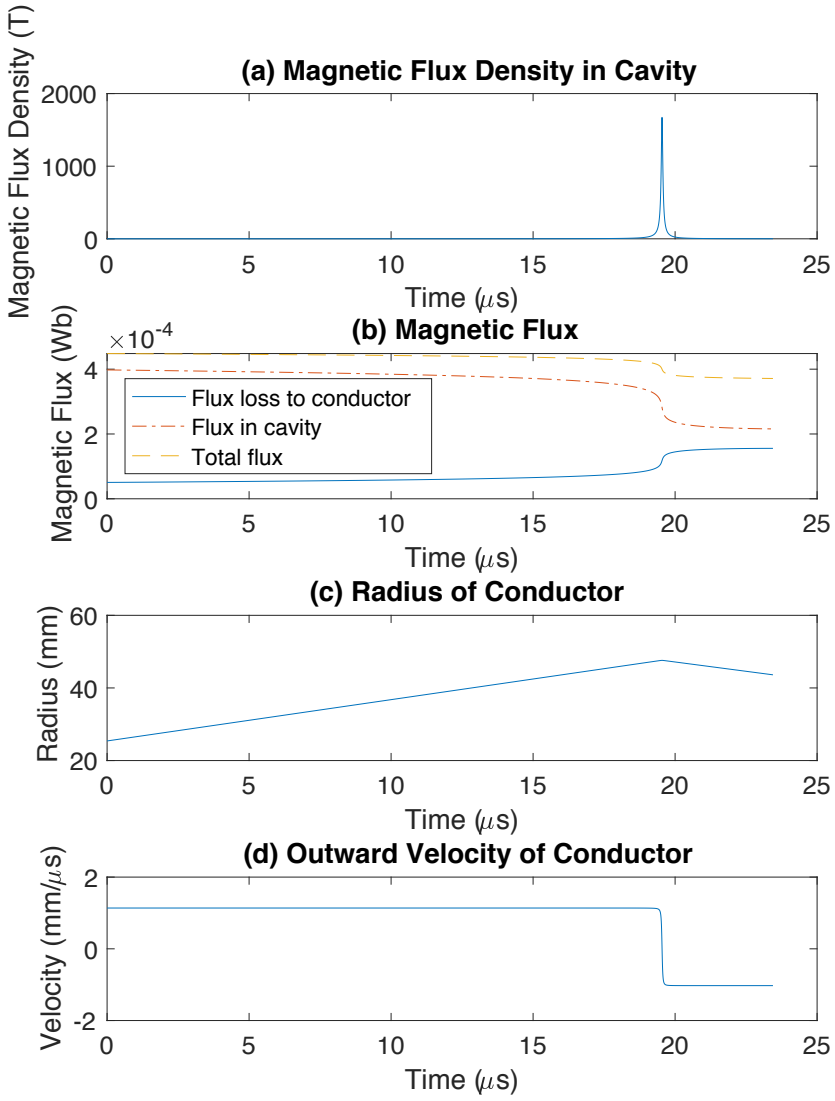

Figure 3-9: Dynamics of a theoretical, indestructible, unloaded loop FCG. The parameters used in this simulation are summarized in Table 3.2. Plot (a) shows the magnetic flux density (B) as a function of time. The simulation has been allowed to continue beyond the point that the magnetic pressure within the cavity exceeds the ultimate tensile strength of the conductor as if the conductor remained together. Plot (b) shows the flux in the cavity ($B \cdot A$), in the conductor (λ_{cond}), and in total in the device (λ_{total}) as a function of time. Plot (c) shows the radius of the conducting cylinder (r) as a function of time. Plot (d) shows the outward radial velocity of the conducting shell ($v_s = \dot{r}_s$) as a function of time.

pressure will oppose it. Indeed, one can see in Figure 3-8d that the velocity of the conductor is beginning to decrease. Figure 3-9 shows the results of the same simulation, allowed to predict past the point that the magnetic pressure exceeds the ultimate tensile strength of the conductor. One can see that turnaround is predicted, just as in the case of the cylindrical implosion generator, but reaching a higher flux density and in a shorter-lived pulse. Based on these results, one would expect plasma generation if an unloaded loop generator were to survive long enough. Figure 3-4d and Figure 3-8d also highlight a limitation of the particular model put forward in these two sections, in that they ignore elastic forces opposing deformation, so the conductor is allowed to expand and contract indefinitely. This limitation, however, has little effect during normal operation and one can remedy this issue to first order by adding another term to the Newton's Second Law equation opposing expansion and contraction.

Figure 3-8b shows once more that as the magnetic field peaks, the total flux begins to dip and the flux in the cavity begins to become a smaller proportion of the total flux. While this change is less pronounced than in the case of the cylindrical implosion generator, the flux in the cavity makes up a smaller proportion of the total flux in this case, meaning diffusion has a larger effect on the generator dynamics.

3.7 Field Exterior to Device — Dipole Analysis

To conclude this chapter, we consider the field exterior to the device and provide an important, but little discussed result (indeed, this author has not seen its mention in existing literature, but finds it hard to believe that it has not previously been discovered). Up until this point, we have developed a model for the magnetic field interior to the device cavity. A reasonable extension would be to consider the field outside the cavity, though still in the near field. We will see that at as soon as the field is measured far enough away that the device can be modeled as a magnetic dipole, flux compression has no effect.

For a magnetic field sensor to be in the far field, the distance between the source

and the sensor must be much greater than both the wavelength of the pulse and the largest length scale of the source. Flux compression generators produce pulses with durations on the order of microseconds. Even if the pulse only lasted a single microsecond, the wavelength would still be about $300\,m$. The maximum length scale of an FCG is much less than $300\,m$, often less than even $1\,m$, especially for modern "minigens" with maximum length scale less than $10\ cm$. So, any sensor placed much less than $300\,m$ away and much farther than $10\,cm$ away from a minigen is in the near field and the generator can be modeled as a simple magnetic dipole.

The magnetic field from a dipole is given by

$$\mathbf{B}(\mathbf{r}) = \frac{\mu_0}{4\pi}\frac{3\hat{\mathbf{r}}(\hat{\mathbf{r}}\cdot\mathbf{m}) - \mathbf{m}}{|\mathbf{r}|^3}, \tag{3.62}$$

where $\mathbf{r}$ is the displacement from the dipole and $\mathbf{m}$ is the magnetic moment of the dipole. For a planar current loop, the dipole moment is given by $\mathbf{m} = i\mathbf{A}$, where i is the current flowing through the loop and $\mathbf{A}$ is a vector with magnitude equal to the area of the loop and direction normal to the plane of the current loop, with a right-handed orientation with respect to the current direction. One can show that this formula still holds true in the case of a generalized cylinder (i.e., the extrusion of a planar curve in a direction normal to the plane in which it lies) and so applies to our flux compression generators.

The magnitude of the dipole moment can then be rewritten as $m = iA = \frac{l}{\mu_0}BA$, where B is still the magnetic field in the cavity. Note, however that the product BA is the flux within the cavity. Indeed, the field at this distance scale from a $+\hat{\mathbf{z}}$ directed FCG is given by

$$\mathbf{B}(\mathbf{r}) = \frac{l}{4\pi}\frac{3\hat{\mathbf{r}}(\hat{\mathbf{r}}\cdot\hat{\mathbf{z}}) - \hat{\mathbf{z}}}{|\mathbf{r}|^3}\lambda_{cavity}, \tag{3.63}$$

where λ_{cavity} is the flux in the cavity. While the magnetic field within the cavity increases due to flux compression, the flux within the cavity does not increase, even decreases slightly with diffusive losses. So, while FCGs are capable of creating mega-gauss magnetic fields, these are only internal to the device. As soon as the field is measured far enough away that the generator emits like a dipole, there are no

magnetic field gains from flux compression. In fact, at this distance, one cannot tell purely by examining the field if flux compression is occurring. Note that this is a separate phenomenon from the $1/r^3$ die-off of magnetic fields from dipole sources. One cannot use FCGs to generate large magnetic fields not in the immediate vicinity of the device. Only close enough that features of the generator are comparable in scale to the distance from the generator will any effect of flux compression be noticeable, which both precludes the use of an unloaded FCG for even such near-field magnetic field generation (despite the immense field generation within the device) and puts a significant constraint on any inductively coupled load.

3.8 Summary and Conclusions

This chapter has presented a new model for flux compression generators in the shape of a generalized cylinder, represented by eqs. (3.47) to (3.49). This model differs from the conventional circuit model in its more rigorous treatment of magnetic diffusion, without going as far as calculating the fields throughout the entire device (which would certainly require greater specification in generator topology and likely require finite-element analysis). In topologies more dominated by diffusion and in lower speed experiments, this model should yield more accurate results than the common practice of a linearly decreasing skin-depth. Heuristically, those topologies with cavities with higher surface-area-to-volume ratios would be more influenced by diffusion, and so benefit more from this model. Consequently, the cylindrical implosion generator considered in section 3.5 should be the least influenced by magnetic diffusion of all generators in the shape of a generalized cylinder, providing a lower bound for usefulness of the model proposed in this chapter.

To demonstrate the model, section 3.5 considered the cylindrical implosion generator, represented by eqs. (3.51) to (3.55). This model also demonstrates the extensibility of the general model by showing how one might account for the effect of magnetic pressure, but ignore elasticity. The results of simulating this model are shown in Figure 3-4.

To further demonstrate the model, section 3.6 considered the loop generator, represented by eqs. (3.56) to (3.61). To model this generator, an additional reservoir of flux had to be considered into which flux could no longer diffuse, yielding an extra equation. The results of simulating this model are shown in Figure 3-8.

Finally, in section 3.7, it was shown that the magnetic field in the near-field, but far enough a way that the generator seems small, shows no evidence of flux compression, as seen in eq. (3.63). While the field within the generator increases to great values, the field external to the device is scarcely affected. Despite the implications of this effect, it receives little to no mention in literature reviewed by this author.

Chapter 4

Seed Current Source

Flux compression generators are fundamentally current amplifiers. FCGs compress an existing flux to increase the strength of the magnetic field and the current, but do not themselves produce the initial flux. As such, any complete FCG system requires a seed current source to provide the initial flux.

While FCG operation is agnostic to the means of generating the initial flux — in particular, the ideal flux compression generator has no memory of the past flux — most seed current sources provide current pulses. There are several reasons behind the employment of an initial current pulse, rather than a slow flux build-up. A slower generation of flux will result in larger diffusive losses from the input, and so is less efficient than delivering the same current in a pulse. Secondly, to maximize current output of the FCG, the input current should also be maximized, and it is often easier and more energy efficient on the input side to create a pulse of high current than to sustain a high current as it builds. Furthermore, maintaining a high current poses practical issues in terms of the current capacity of cabling; this must be taken into account to ensure any cables carrying high currents do not melt from Joule heating. Finally, the large magnetic fields created by the initial current pulse lead to large magnetic forces that put strain on the generator; maintaining these fields for longer durations of time increases the potential deformation caused by the magnetic forces as well as the likelihood of failure [1]. Indeed, these forces can be so strong that to counter them, some researchers have encased their stators in concrete to hold the

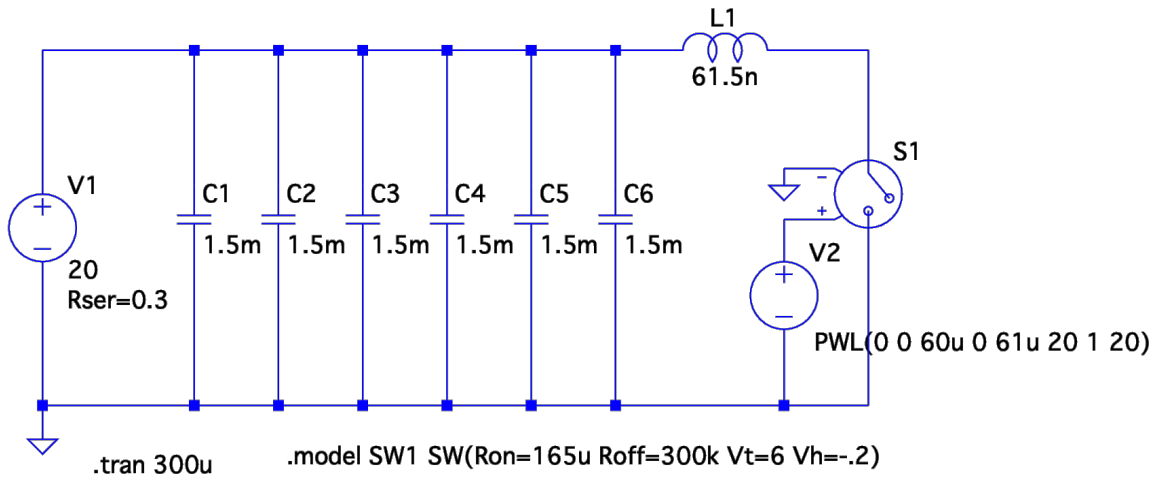

Figure 4-1: Schematic of capacitor bank design. A 20 V source charges six parallel capacitors, each 1.5 mF. After 60 μs, the switch flips from open to closed (taking 1 μs to do so), allowing the capacitors to discharge into the inductor, which models the loop generator designed in Chapter 5. Results of the simulation run in LTSpice are shown in Figure 4-2.

generator together [25].

Historically, the seed source technology most commonly employed in FCG systems has been the capacitor bank [1]. Some recent systems have used explosive pulsed power sources such as the ferromagnetic generator [13] or the ferroelectric generator. In the remainder of this chapter, we first consider the capacitor bank as a seed current source and a design for a capacitor bank is presented to seed the loop generator designed in Chapter 5. Then, the ferromagnetic generator is examined, along with a brief description of the ferroelectric generator.

4.1 Capacitor Bank

Capacitors provide for easy storage and rapid discharge of electrical energy. A great amount of energy can be stored in large capacitors, even at a low voltage. Indeed, for the design presented in this section, the supply voltage was limited to 20 V, which can be readily and simply supplied, though many capacitor banks operate at higher voltages. The advantage of higher voltages is that they would require smaller

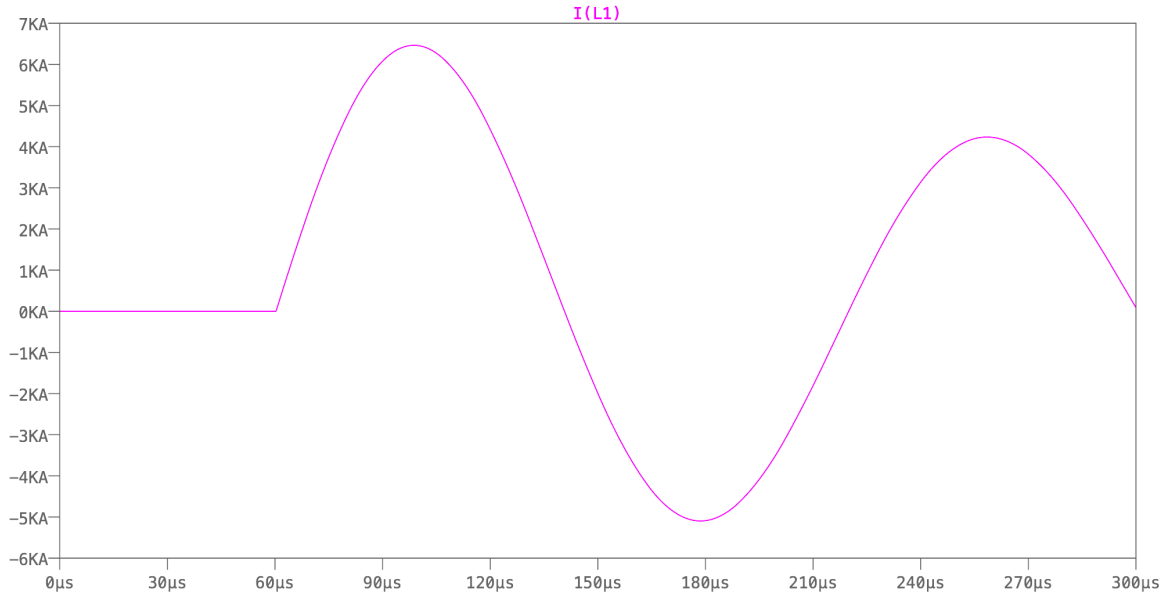

Figure 4-2: Current in the generator (L1) from capacitor bank pictured in Figure 4-1. For the first $60\mu s$, the switch is open, after which the switch closes (taking $1\,\mu s$ to do so). At this point the capacitors can discharge into the inductor, so the current in the inductor increases. After $38\,\mu s$ of discharge, the current in the inductor has reached its maximum value of 6.5 kA. At this point, the detonation would begin before the current begins to decrease again. Simulation run in LTSpice.

capacitors to store the same energy, thus reducing seed pulse time and associated losses. For this reason, there are also designs for capacitor bank systems that initially charge at a lower voltage and then switch to discharge at a higher voltage. A particular system of this variety is called the Marx generator and relies on spark-gap voltage breakdown to produce a large initial current pulse [11].

The schematic for the capacitor bank here presented is shown in Figure 4-1. The 20 V supply, V1, charges the capacitors, C1 through C6, as the switch, S1, begins open. After the capacitors are fully charged, S1 closes, connecting the generator, L1, to the capacitor bank. The inductor, L1, represents the loop generator design presented in Chapter 5; for design parameters see Table 5.1. Since there is now a positive voltage across L1, its current begins to increase, drawing energy from the capacitors. Figure 4-2 shows the current in L1 as the capacitors discharge to be a damped sinusoid. The maximum current is reached roughly after a quarter period. At this point the flux is maximized, so the explosives in the generator are detonated

and the input is sealed off, trapping the flux in the generator to be compressed. As shown in Figure 4-2, the current increase slows as the maximum is approached, so some designs will seal detonate slightly prior to peak current, as this is the point that resistive losses are highest (since the current is at its highest) and there is marginally less flux to be gained by waiting longer [1].

Let the inductance of the generator prior to detonation be L, the voltage supply be V, the total capacitance of the cap bank be C, the peak current in the generator be I, and the peak flux in the generator from the seed current be $\Lambda = LI$. Suppose only 70% of the energy in the capacitor bank transfers to the inductor; then,

$$\frac{1}{2}LI^2 = \frac{\Lambda^2}{2L} = 70\% \cdot \frac{1}{2}CV^2.$$

So, the current in the generator is given by,

$$I = \frac{V}{\sqrt{\frac{L}{C}}} \cdot \sqrt{70\%},$$

and the flux is given by,

$$\Lambda = V\sqrt{LC} \cdot \sqrt{70\%}.$$

If the generator's cavity initially has area A, the initial field is then given by,

$$B = \frac{V\sqrt{LC}}{A} \cdot \sqrt{70\%}.$$

The generator presented in Chapter 5 has initial inductance $L = 61.5\,nH$ and initial area $A = 30.4\,cm^2$. To produce a 0.13 T initial flux (specified by Draper), the capacitor bank must have capacitance

$$C = \frac{1}{L \cdot 70\%}\left(\frac{BA}{V}\right)^2 = 9\,mF.$$

As shown in Figure 4-1, we produce this with a parallel combination of six 1.5 mF capacitors. The capacitors chosen for this reference design are B25620B0158K883 from EPCOS (TDK Electronics). These film capacitors were chosen for their large

capacitance and low ESR ($1.1\,m\Omega$) and ESL ($\leq 60\,nH$). Since we expect $I = 6.4\,kA$ total, less than $1.1\,kA$ will come from each capacitor, so the voltage drop associated with the ESR of each capacitor is less than 1.2 V, which is acceptable on a 20 V rail and not going to severely limit current capacity of the circuit.. The generator has series resistance given by $2\pi\left(\sigma l \log\left(1+\frac{w}{r_l}\right)\right)^{-1} = 15.8\,\mu\Omega$, where σ is the conductivity of copper, l is the height of the generator, w is its thickness, and r_l is the radius of the outer loop. The design of the generator is given in Chapter 5, but, here, this calculation shows the generator to provide negligibly to the series resistance. The parallel combination of the equivalent series inductances from the six capacitors is at most 10 nH, which is six times less than the inductance of the generator.

The switch implementation must be able to carry 6.4 kA for a $\frac{\pi}{2}\sqrt{LC} = 37\,\mu s$ pulse. (Technically, the full 6.4 kA is not carried for the whole duration of the pulse, but it is safer to require the full current over the full pulse.) This specification can be achieved by a parallel combination of IGBTs. The specific IGBT chosen is the IXGK400N30A3, which can carry 400 A continuously. To carry the full 6.4 kA with a bit of headroom, 20 IGBTs are connected in parallel, able to carry a combined 8 kA. Each IXGK400N30A3 gate requires 560 nC to switch, so a total of $11\,\mu C$ of charge must be provided by the gate driver. The MIC4452 gate driver can supply 12 A of current, switching all the IGBTs in $0.93\,\mu s$. At this level of current, the IGBTs each have transconductance of 300 S, so the parallel combination has transconductance 6 kS and on-resistance $167\,\mu\Omega$. When the collector-emmiter voltage of the IGBT is 300 V and the gate is connected the emitter, $50\,\mu A$ of current flow, so the off-resistance of each IGBT can be estimated as $6\,M\Omega$, leading to a combined switch off-resistance of $300\,k\Omega$.

We now see that Figure 4-1 shows the schematic of an LTSpice simulation for this system, including ESR and ESL of the capacitors, the calculated on- and off-resistances of the switch implementation, and the ESR of the generator. The current in the generator is shown in Figure 4-2. The simulation predicts a maximum current of 6.5 kA and a $38\,\mu s$ rise time, which closely matches the results estimated assuming 30% energy losses.

While we have shown this capacitor bank to meet the electrical requirements of the system, it requires six B25620B0158K883 capacitors. Each of these capacitors has an 11.6 cm diameter and 18.1 cm height, so the capacitor bank takes up substantially more volume than the FCG and undermines the miniaturization effort. Such large capacitors were necessary, however, to generate such a large initial field and to keep down the ESR and ESL of the capacitor bank. In the next section, we consider an alternative that can be designed to be more compact.

4.2 Ferromagnetic and Ferroelectric Generators

Explosives have a much higher energy density than capacitors ($8000\,MJ/m^3$ compared to $0.1\,MJ/m^3$) , and so provide opportunity for a more compact seed current source [12]. The ferromagnetic generator (FMG) is another explosive pulsed power technology, but — unlike the FCG — is a current source — rather than a current amplifier. FMGs provide current by demagnetizing permanent magnets within conducting loops. The changing flux induces a current in the conducting loop. Demagnetization is achieved by exposing the permanent magnets to an explosive shock wave.

When a shockwave longitudinally compresses $Nd_2Fe_{14}B$ magnets with a pressure of 28–38 GPa, the magnets demagnetize nearly completely [26]. Both [26] and [27] calculate the necessary pressure for demagnetization, with the latter also specifying partial demagnetization pressures: 36% demagnetization at 9 GPa and 44% at 14 GPa. These shock wave pressures are obtained either by detonation of the explosives directly on the magnets, or by collision with a flyer plate propelled by the explosives.

In [13], a loop FCG is seeded with an FMG of comparable size (pictured in Figure 4-3). Detonation of a high explosive surrounded by a $Nd_2Fe_{14}B$ ring demagnetizes the ring, producing a current in the FMG. This current produces flux the loop FCG. When the high explosive in the FCG detonates, the flux is compressed and the current is amplified. Finally, the amplified current from the FCG flows into the load loop.

The ferroelectric generator (FEG) operates on the same principle, except that

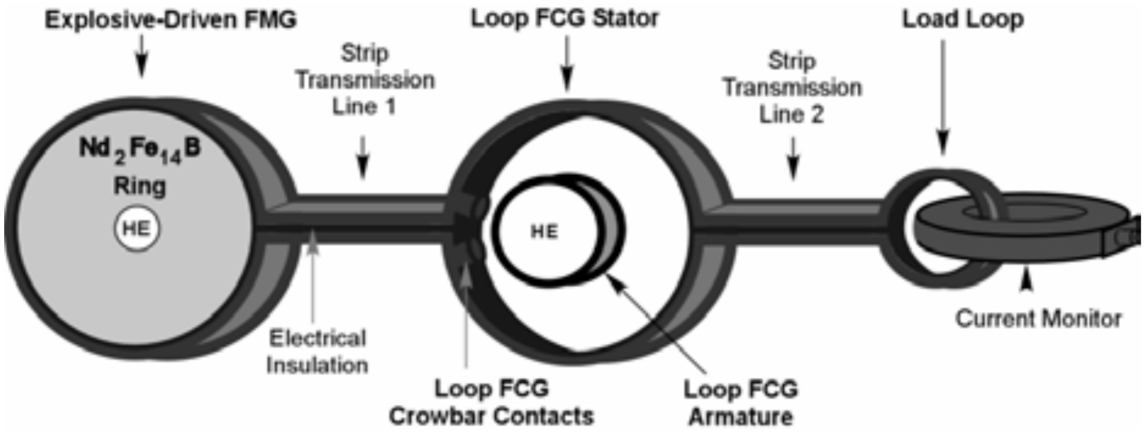

Figure 4-3: FMG-FCG system from [13]. Detonation of a high explosive surrounded by a $Nd_2Fe_{14}B$ ring demagnetizes the ring, producing a current in the FMG. This current produces flux the loop FCG. When the high explosive in the FCG detonates, the flux is compressed and the current is amplified. Finally, the amplified current from the FCG flows into the load loop.

ferroelectric and piezoelectric materials are used instead of ferromagnetic materials. Research has also shown that FEGs operate better when depolarization pressures are below shock-wave pressures, preventing ceramic fractures and electrical breakdown [7].

For more information of FMGs or FEGs, see [7].

4.3 Summary and Conclusions

This chapter has discussed both the conventional capacitor bank and modern, explosive ferromagnetic and ferroelectric generators as current sources to provide the seed-current for a flux compression generator. In the case of the capacitor bank, a reference design is provided, tailored to powering the loop generator design presented in Chapter 5, outlined in Table 5.1. This reference design exemplifies a problem with the use of capacitor banks in systems with size constraints: the capacitor bank is larger than the minigen it powers. This limitation motivates the use of more compact seed-current sources, such as the explosively-powered ferromagnetic and ferroelectric generators described in section 4.2.

Chapter 5

Loop Generator Design and Experimental Setup

In this chapter, a loop FCG design is presented along with the design of an experiment to test the generator by sensing both the field and the flux within the device. The first section details the construction parameters of the generator and states simulated results of running the generator. The following section discusses how the generator might be tested, including a design for a custom, though simple, magnetic field sensor.

5.1 Loop Generator Design

Table 5.1: Design parameters for loop generator

Parameter	Symbol	Value
Loop inner radius	r_l	1.75 in.
Shell inner radius	r_{s0}	1 in.
Loop and shell wall thickness	w	0.25 in.
Loop and shell center displacement	δ	0.375 in.
Height	l	2 in.
Material		Copper (C101) [22]

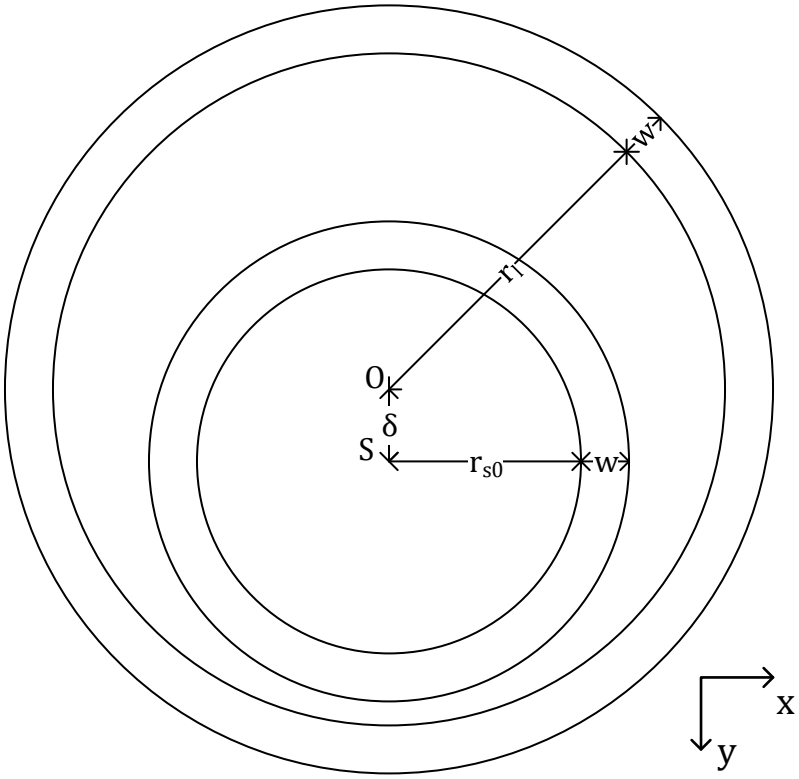

Figure 5-1: Geometry of Loop Generator. The geometry of the generator is shown. The width, w, of both the loop and the shell is 1/4 in. The inner radius of the loop, r_l, is 1.75 in. The inner radius of the shell, r_{s0}, is 1 in. The separation, δ, between the centers of the loop and shell is 3/8 in. Additionally, the height, l, of the generator is 2 in. out of the page.

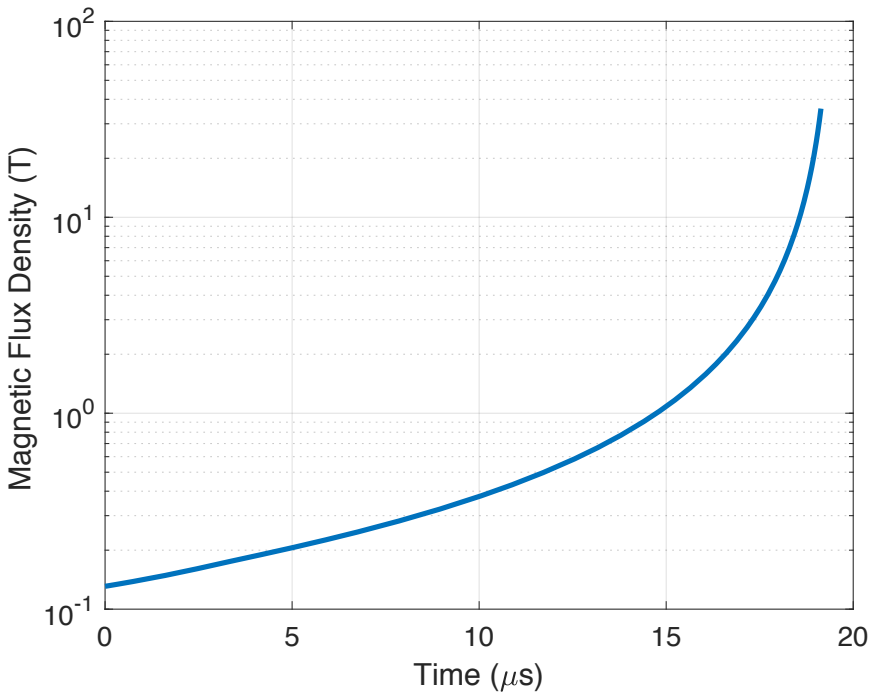

Figure 5-2: Simulated Magnetic Field within Generator. The generator here described was simulated with the model developed in Chapter 3. Here, the time-evolution of the magnetic field within the cavity is shown on a log scale.

As seen in Table 5.1, the loop generator presented here has loop inner diameter 3.5 in., shell initial inner diameter 2 in. (both with thickness 1/4 in.), and height 2 in., and separates the centers of the loop and shell by 3/8 in. The geometry is shown in Figure 5-1. When choosing the inner diameter and thickness of the shell and loop, one must take into consideration the availability of copper pipes with those dimensions, as machining custom pieces significantly increases the cost. Simulations of this design in section 3.6 showed it to meet proprietary specifications provided by Draper. The magnetic field predicted by that simulation is shown again here in Figure 5-2. The simulation was ended when the magnetic pressure within the device exceeded the ultimate tensile strength of copper, but it is possible that failure occurs sooner, resulting in a lower maximum magnetic field than the 36 T predicted here. The predicted half-width at half-max (HWHM) of the pulse is $0.24\,\mu s$.

Figure 5-3 shows an initial CAD of the FCG. The shell is filled with high explosive and held in place by the plastic retainer shown in white. In the design presented here,

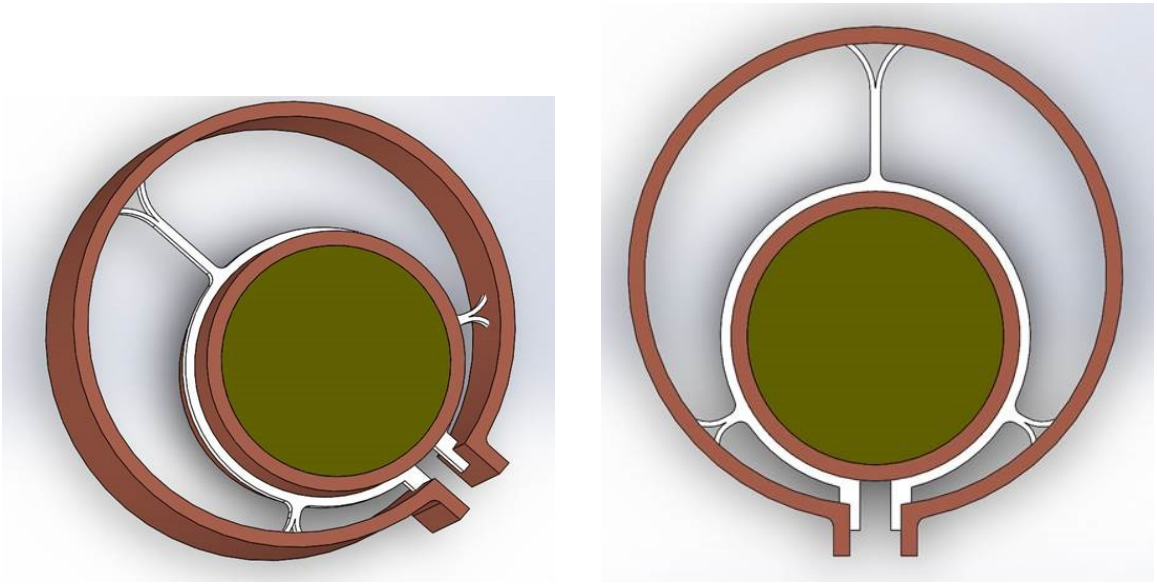

(a) Angled View. (b) Top View.

Figure 5-3: CAD of Loop Generator. The shell is filled with high explosive and held in place by the plastic retainer shown in white. The retainer is designed to provide minimal resistance to the expansion of the shell. CAD by Katherine Graham of Draper.

the high explosive is C-4. Filling the shell requires $\pi r_{s0}^2 l \rho_{C4} = 0.16\,kg = 0.36\,lb$ of C-4, where ρ_{C4} is the mass density of C-4, $1.59\,g/cm^3$ [23].

Figure 5-4a shows the final CAD of the loop, with holes for attaching the seed-current source. Figure 5-4b shows the fabricated loop. The loop was milled from a copper pipe with an outer diameter of 4 in. and thickness of 1/4 in. The slit is 1 cm wide.

The fabricated shell, an off-the-shelf copper pipe with outer diameter 2.5 in. and thickness 0.25 in., is shown in Figure 5-5.

The detonation velocity of C-4 is $8\,mm/\mu s$, so it traverses the device in $2\,in/(8\,mm/\mu s) = 6.35\,\mu s$, finishing long before the device is fully compressed.

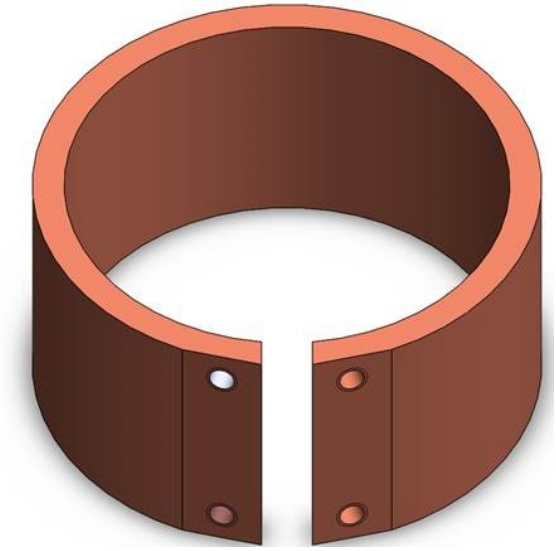

(a) Generator outer loop CAD.

(b) Fabricated generator outer loop.

Figure 5-4: The loop was milled from a copper pipe with an outer diameter of 4 in. and thickness of 1/4 in. There is a 1 cm slit and two holes on each side of the slit to attach the seed-current source. CAD by Carlos Rodriguez of Draper.

Figure 5-5: Loop Generator Shell. The shell is an off-the-shelf copper pipe with outer diameter 2.5 in. and thickness 0.25 in.

5.2 Experimental Setup

5.2.1 Facility

The first point to be considered in an experiment with an FCG is the locale. Since a half-pound-equivalent of TNT is being detonated, the experiment should only be held at a qualified facility. In planning this experiment, a facility belonging to the University of Rhode Island Center of Excellence for Explosives Detection, Mitigation, and Response was selected. Their range is rated up to 30 lb. of TNT, far above the explosives being used in this experiment. They also provide for the acquisition and proper handling of the explosives. Additionally, there are high-speed cameras on-site for recording the experiment. A high-speed recording of the detonation gives information to verify the speed of the shell, which was approximated in the last section by Gurney analysis. The recording will also indicate at what point mechanical failure was experienced, something currently unpredicted, but extremely important for predicting maximum field strength and current amplification.

5.2.2 Magnetic Field in Cavity — Close-range Magnetometer

Beyond the high-speed recording, magnetic field strength values must be recorded. Few off-the-shelf magnetometers capture up to the frequencies encountered in this sub-microsecond pulse and those that do are generally quite expensive. Instead, two custom, yet simple, magnetometers were designed. The close-range magnetometer consists of a pick-up coil, an integrator, the logarithmic amplifier U1(AD8310ARMZ), a non-inverting amplifier with op-amp U2 (LTC6292-10), and an ADC (AD9262), as shown in Figure 5-6. The voltage across the pick-up coil is $v_L = \frac{\mathrm{d}(BA)}{\mathrm{d}t} = \dot{B}A$, where B is the average magnetic field in the loop and A is the area of the loop. If the area is small enough, the field can be assumed uniform and B is then the local magnetic field. Assuming the time constant R_1C is much longer than the duration of the pulse, the voltage across the capacitor is then $v_C = \frac{A}{R_1C}B$. As seen in Figure 5-2, the magnetic

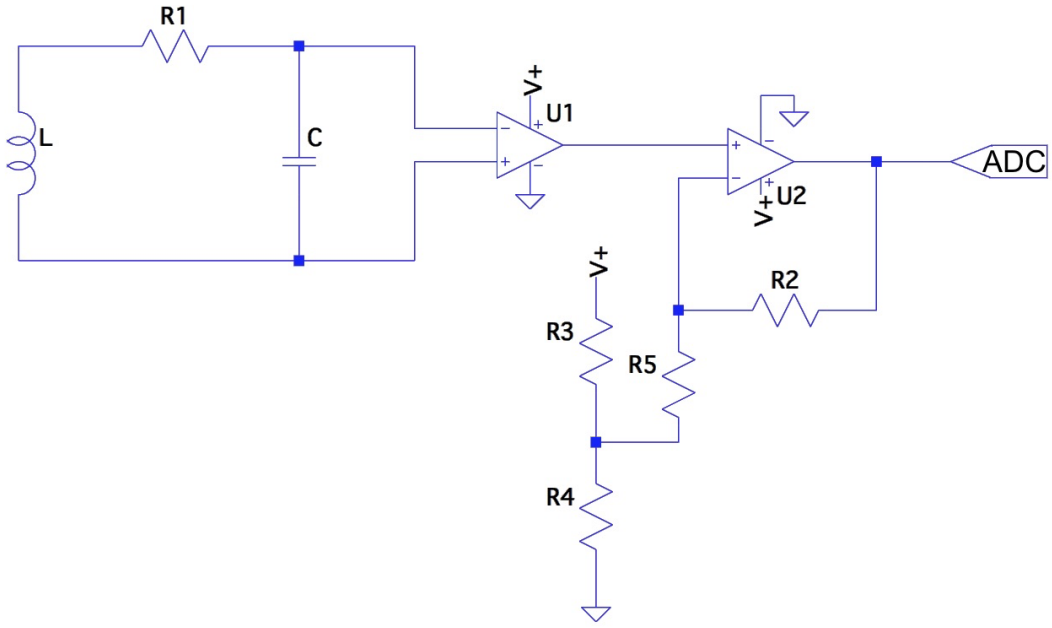

Figure 5-6: Close-range Magnetometer Schematic. The magnetometer consists of a pick-up coil (L), a simple RC integrator, a logarithmic amplifier (U1, AD8310ARMZ), a non-inverting amplifier (made with U2, LTC6292-10), and an ADC (AD9262).

field in this case is most naturally considered on a log-scale. To increase the dynamic range of the magnetometer, the integrated signal is fed into a logarithmic amplifier. The AD8310ARMZ amplifier is chosen for its high frequency response and ability to detect DC signals. The maximum allowable input to the amplifier is 2.2 V.

Due to the high magnetic field strengths within the device, the pick-up coil is specified to be single-turn with radius 1 cm. Even then, if the magnetic field reaches the full 36 T, the time constant would need to be $R_1 C = \frac{BA}{v_c} = 5.14\,ms$. A time constant of 5.1 ms can be achieved with a $1\,M\Omega$ resistor (R1) and a $5100\,pF$ capacitor (C). Because the effects of flux compression are not seen significantly outside the device, this coil must be placed in close proximity to the generator, so that it will not see the generator as a dipole (see section 3.7). The expected output of the logarithmic amplifier is shown in Figure 5-7, assuming the magnetic field in the coil is equal to that in the cavity.

The analog signal must now be converted to the digital domain for storage and analysis. A high-speed ADC is necessary to be sure to capture multiple samples during the $0.24\,\mu s$ pulse, so the AD9262 is selected. This 16-bit ADC can collect 160

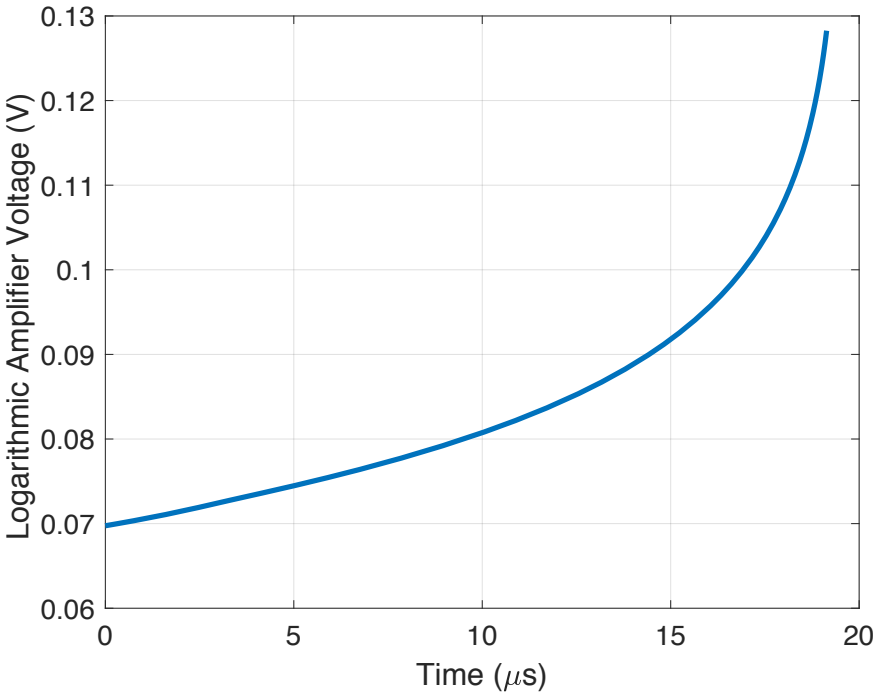

Figure 5-7: Magnetometor Logarithmic Amplifier Expected Output Signal. The voltage output of the logarithmic amplifier is shown.

MSPS, so 38 samples in $0.24\,\mu s$, or 19 samples from each of two channels (one for the field sensor and one for the flux sensor). With its evaluation board, this ADC can be plugged into a computer for USB data-capture, simplifying the magnetometer data acquisition system design. Since the ADC has an input range of 2 V p-p, the output of the logarithmic amplifier can be fed into a non-inverting amplifier with a gain of 25 and a 0.06 V shift in offset ($v_{OUT} = 25(v_{IN} - 0.06\,V) + 0.06\,V$) to utilize the full range of the ADC. This amplifier can be implemented with a LTC6269-10 op-amp (U2) and resistors such that $\frac{R_4}{R_3+R_4}V^+ = 0.06\,mV$, $\frac{R_2}{R_5} = 24$, and R3 and R4 are much less than R2 and R5, to provide a stiff reference for the amplifier. This dual op-amp was chosen particularly for its high gain-bandwidth product of 4 GHz. With a gain of 25, the op-amp has bandwidth 160 MHz and the ADC can only resolve frequencies up to 40 MHz, since it samples this channel at 80 MSPS. The results of such amplification are given in Figure 5-8. While a larger gain could have been chosen to utilize more of the ADC's range, setting the floor a bit above zero allows for the field to be lower than expected, since the loop would not survive being placed within the cavity long

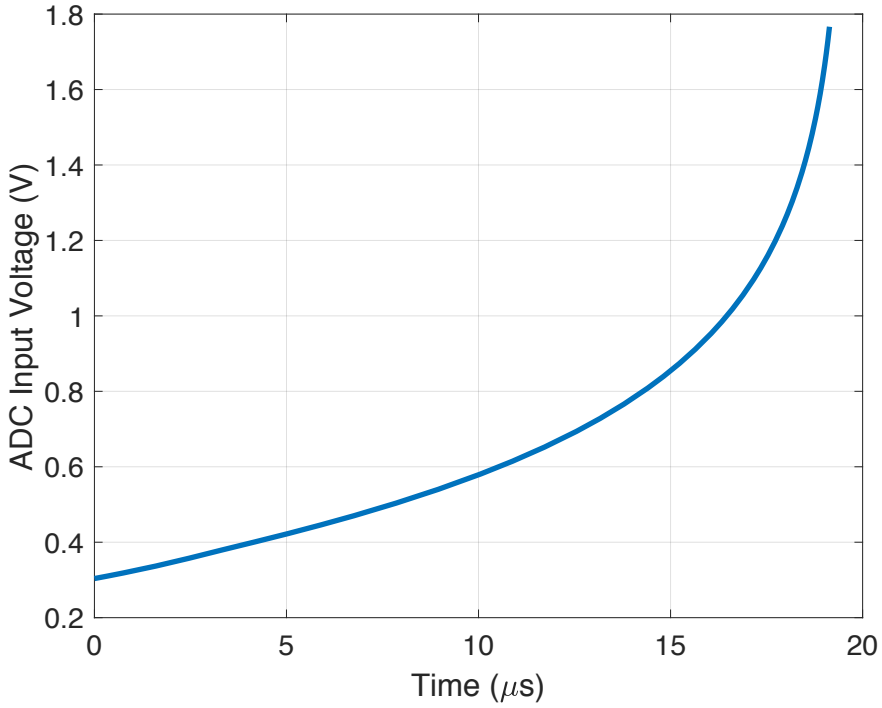

Figure 5-8: Magnetometor ADC Input Signal. The voltage at the analog input of the magnetometer ADC is shown. This is the logarithmic amplifier voltage after amplification and offset-shifting by a non-inverting amplifier.

enough to capture data.

5.2.3 Flux in Cavity — Far-range Magnetometer

To track the flux within the device, one can place a more sensitive magnetometer farther away. A schematic for this magnetometer is shown in Figure 5-9 and has the same design as the up-close magnetometer except for different values and the omission of the logarithmic amplifier. With this magnetometer, one can reproduce the "Flux in cavity" plot from Figure 3-8 (b), since the field at a distance away is determined by the flux in the cavity, not the field in the cavity. From the results of section 3.7, the expected magnetic field at 3 m away is pictured in Figure 5-10.

Replacing the $1\,M\Omega$ resistor (R1) with a $1\,k\Omega$ resistor and increasing the magnetometer coil to a 15 cm radius with 10 turns puts the voltage at the output of the integrator in the 13–17 mV range, as shown in Figure 5-11.

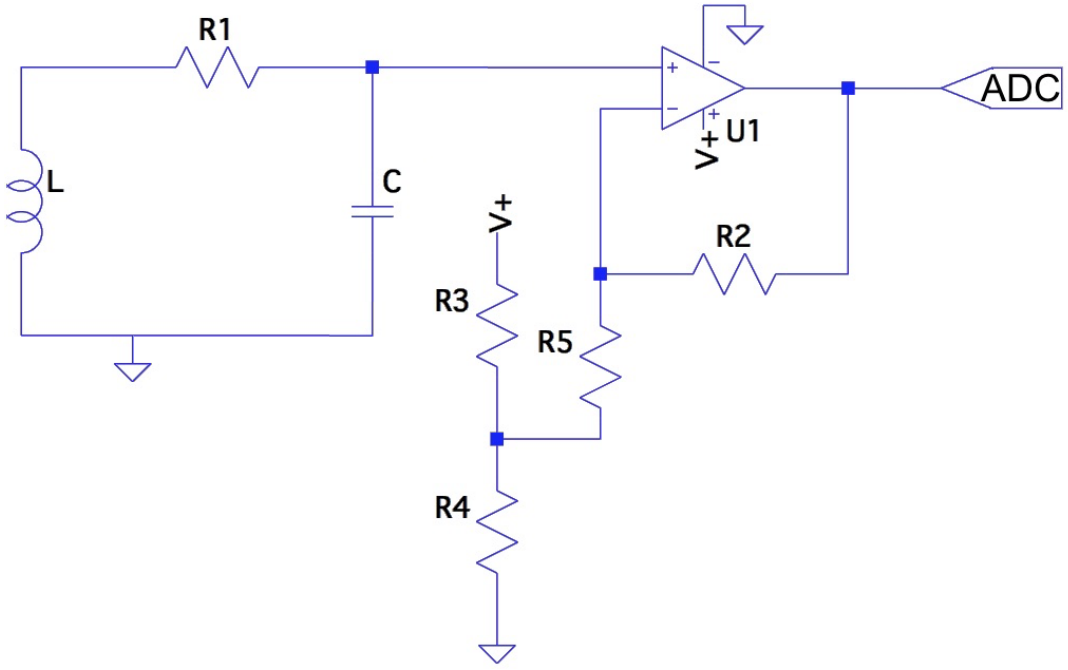

Figure 5-9: Far-range Magnetometer Schematic. The magnetometer consists of a pick-up coil (L), a simple RC integrator, a non-inverting amplifier (made with U1, LTC6292-10), and an ADC (AD9262). By sensing the magnetic field farther from the device, the flux within the device can be indirectly measured.

Amplifying this voltage with a gain of 100 and a voltage offset of 13 mV ($v_{OUT} = 100(v_{IN} - 0.013\,V) + 0.013\,V$) extends the signal range to 0.1–0.35 V, as shown in Figure 5-12. This amplifier can be implemented with the other op-amp in the LTC6269-10 used in the first magnetometer (U1 of Figure 5-9) and resistors such that $\frac{R_4}{R_3+R_4}V^+ = 0.013\,mV$, $\frac{R_2}{R_5} = 99$, and R3 and R4 are much less than R2 and R5, to provide a stiff reference for the amplifier. With a gain of 100, the op-amp has bandwidth 40 MHz and the ADC can only resolve frequencies up to 40 MHz, since it samples this channel at 80 MSPS. In theory, a higher gain is possible without over-voltaging the chosen ADC, but since the bandwidth of the amplifier has been reached, such a design would require a second amplification stage. Alternatively, the gain of 100 is sufficient, as the full 16-bit granularity of the ADC is unnecessary for a simple verification experiment.

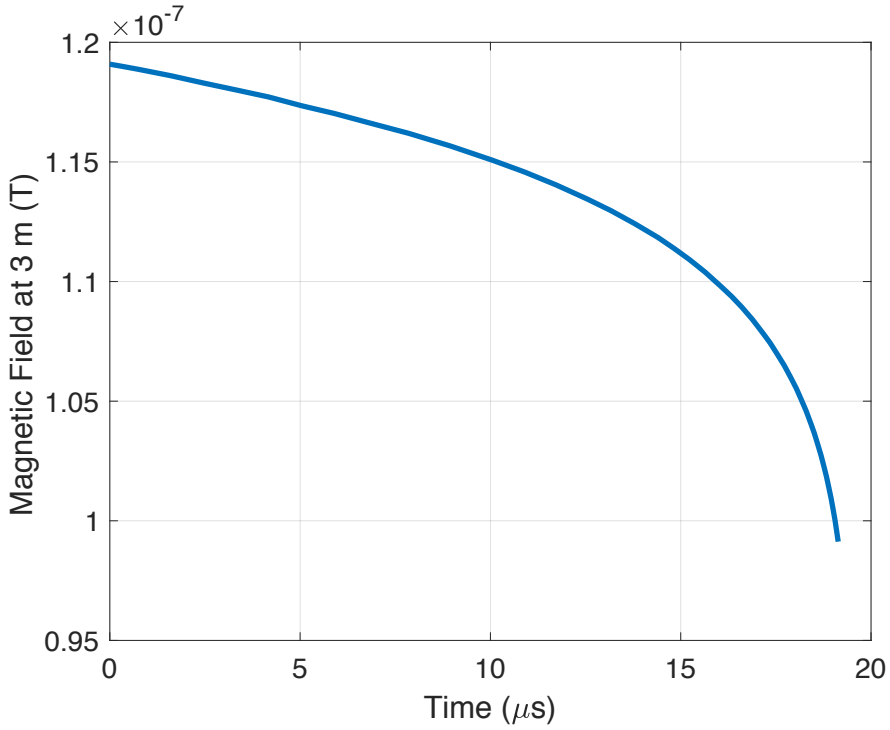

Figure 5-10: Magnetic Field at a Distance. At a distance of 3 m away, the generator looks like a dipole, so the field is a function of the flux in the device, not the field in the device.

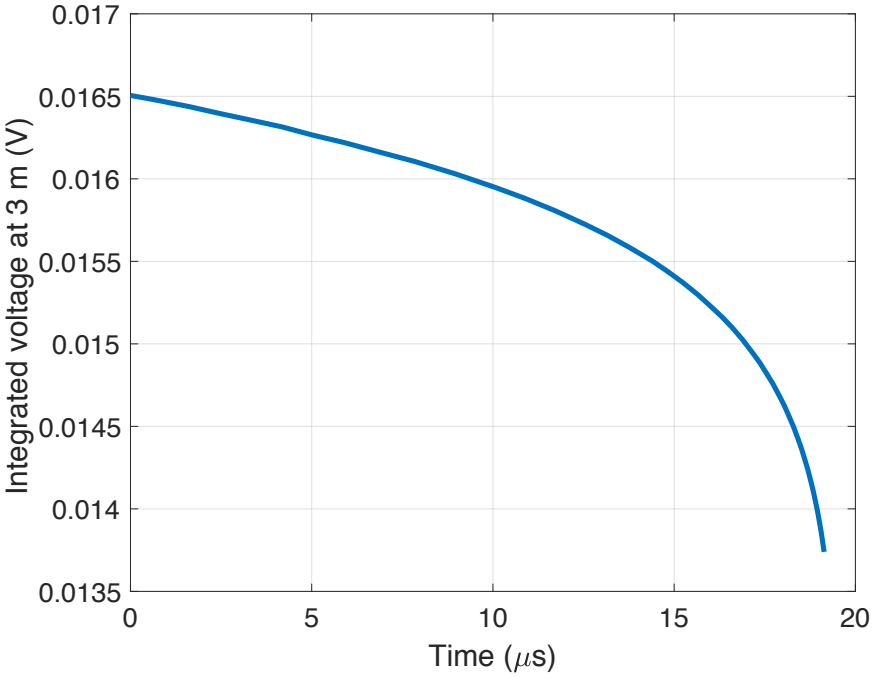

Figure 5-11: Flux-measuring magnetometer integrator output. Using a 1 $M\Omega$ resistor and a 5100 pF capacitor to form the integrator connected to a magnetometer coil with a 15 cm radius and 10 turns yields a voltage at the output of the integrator in the 13–17 mV range and proportional to the flux in the device.

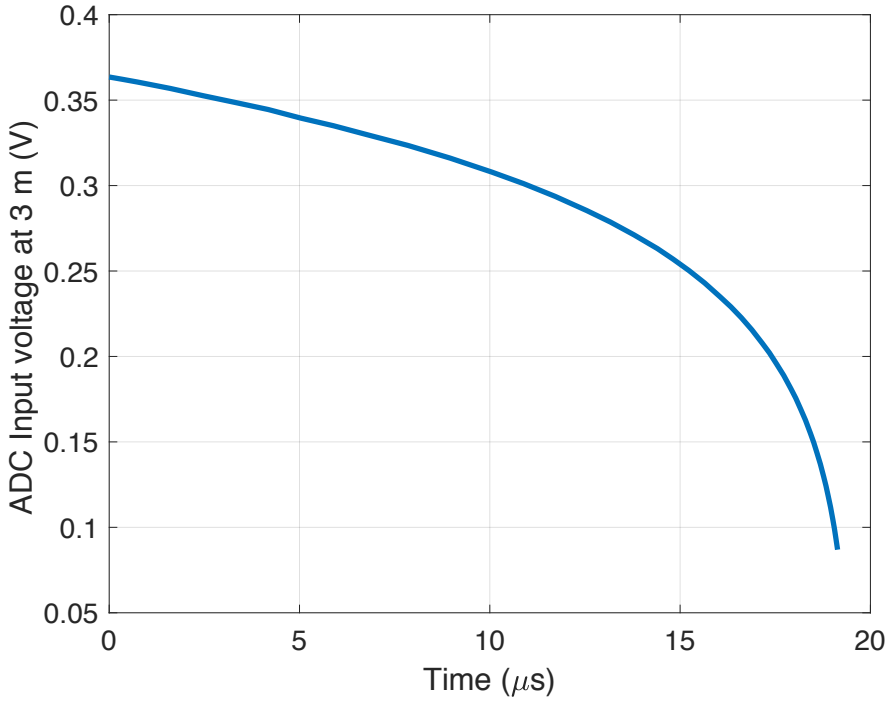

Figure 5-12: Flux-measuring magnetometer ADC input. After amplifying the integrator output, the signal range becomes 0.1–0.35 V.

5.3 Summary and Conclusions

This chapter presents a design for a loop flux compression generator and an experiment to characterize and verify it. Design parameters for the generator are presented in Table 5.1 and were found by trial and error using the model developed in Chapter 3, optimizing for magnetic field strength within the cavity, constrained by the size of the generator and availability of copper pipes of such dimensions. The experimental setup includes the design of two magnetometers: one optimized to measure the magnetic field within the cavity and one optimized to measure the magnetic field far from the cavity, which is proportional to the flux in the cavity. The timing of the pulse is such that radio frequency components are not necessary, but the system is reaching the upper bandwidth limit of standard components, so care must be taken when selecting parts for these magnetometers to ensure the signal remains undistorted.

Chapter 6

Non-explosive Flux Compression Generators

In Chapter 5, a design was presented for an explosively-pumped flux compression generator of the loop variety, along with a description of an experiment to test the system there described. Along with safety concerns stemming from the use of explosives, a potential facility at which to run the experiment was named, due to the fact that the amount of explosives being detonated prevents testing in most lab facilities. While explosives in and of themselves are relatively inexpensive, time at such test facilities and of professionals qualified to safely handle the explosives drive up the development cost of these systems. Non-explosive flux compression generators present great advantages in safety as well as in cost and time of development and cost of transportation of deployed generators. Beyond these benefits, a non-explosive flux compression generator could potentially be reusable. In this chapter, a class of non-explosive FCG topologies is proposed and two examples from this class are given. (In this chapter, FCG will be used to refer to flux compression generators generally, with specification made between explosively-pumped and non-explosive as necessary.)

Non-explosive flux compression generators have been proposed before. In [10], Dickinson proposes a non-explosive FCG based off the common helical generator, using a gas gun to launch a projectile that plays much the same role as the expanding armature in explosively-pumped helical generators (see Chapter 2, Section 8 for a

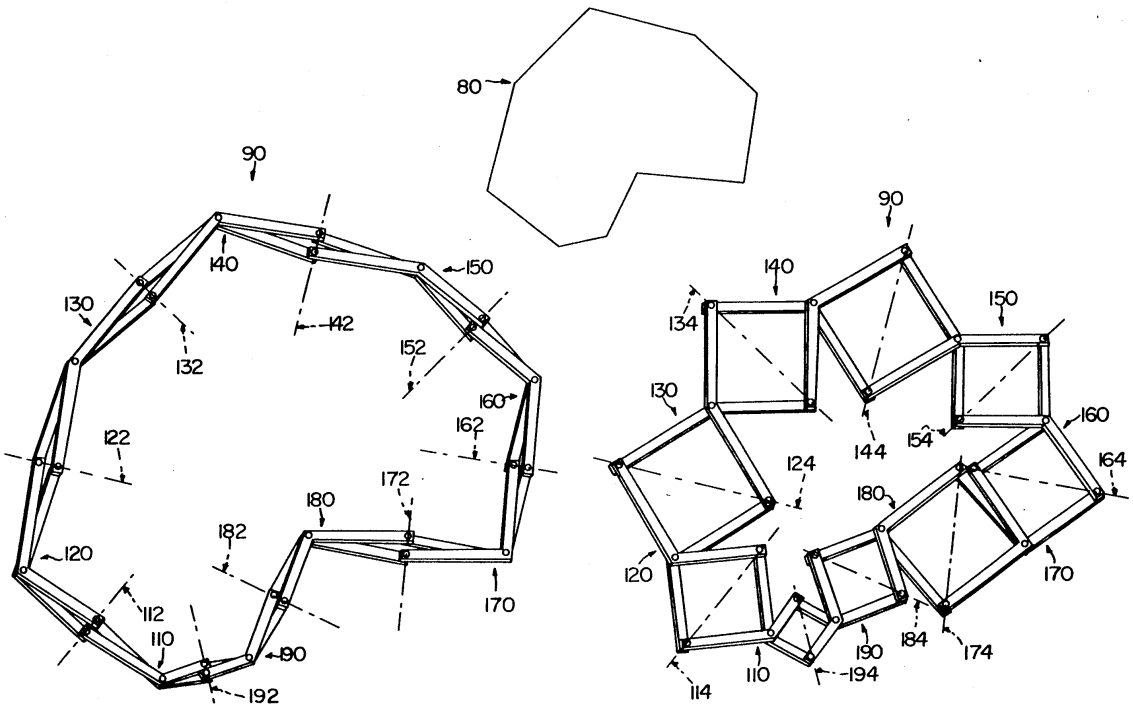

Figure 6-1: Example deployable structure — Hoberman mechanism. The Hoberman mechanism expands and contracts radially by employing a scissor mechanism. By running a current through certain linkages, one can compress flux area by actuating the mechanism. Image from [28].

review of helical generator operation). Every FCG described in Chapter 2 (except for the plate generator — which could be designed with sliding contacts, though often is not) relies on deforming metal to compress the flux area, which requires explosive force. Dickinson avoids deforming metal by launching a metallic projectile that follows the same path as the deforming metal would, creating all the same contacts. Here, we investigate the potential for compressing flux using deployable structures to deform the conducting path without deforming any conductors, only by shifting their positions. This allows for a variety of other forcing mechanisms, such as compressed gas, electronic actuators, or lower/less destructive explosives.

6.1 Deployable Structures and FCGs

A deployable structure is a transformable structure that can autonomously make significant changes to its configuration [29]. Often, these structures have two states — one compact state (typically for easy storage and transportation) and one deployed state wherein their usual operation occurs. Deployable structures are familiar from everyday life, e.g., the umbrella, the folding chair, the retractable roof of a stadium or a convertible, and the scissor lift. A key feature of deployable structures is that they sustain no damage in normal operational transitions between significantly different configurations. They can achieve this by use of coiled rods, flexible shells (such as the tape measure), membranes, and structural mechanisms — assemblies with rigid parts and movable joints, such as the Hoberman Mechanism pictured in Figure 6-1 [29]. This feature makes deployable structures ideal for a non-explosive FCG.

A non-explosive FCG can be designed by replacing any deforming conductors in an explosively-pumped FCG design with deployable structures that can be actuated with far less destructive and dangerous power sources than explosives, e.g., the expansion of a gas. Rather than compressing the flux area (deforming the conducting path) by deforming metal at an explosive rate, a deployable structure can compress the flux area with greater control of the rate of compression. One could even imagine shaping the output waveform by varying the rate of compression. This lower speed increases losses, as the effects of magnetic diffusion are no longer dwarfed by the effects of flux compression. The magnetic Reynold's number for the relevant diffusion problem (studied in Chapter 3) is $R_m = \mu\sigma w u_0$, where μ is the permeability of the conductor, σ is the conductivity of the conductor, w is the thickness of the conductor, and u_0 is the speed of the conductor. As long as the magnetic Reynold's number is greater than unity, flux compression will occur [17]. For 1/8-inch thick copper, this requires the conductor to move at a speed exceeding 4.2 m/s, about four times walking speed. For comparsion, the explosions used in most FCGs are about 500 times faster. So, a non-explosive FCG will experience greater diffusive losses than an explosive FCG, but should easily be able to experience flux compression without producing a shockwave,

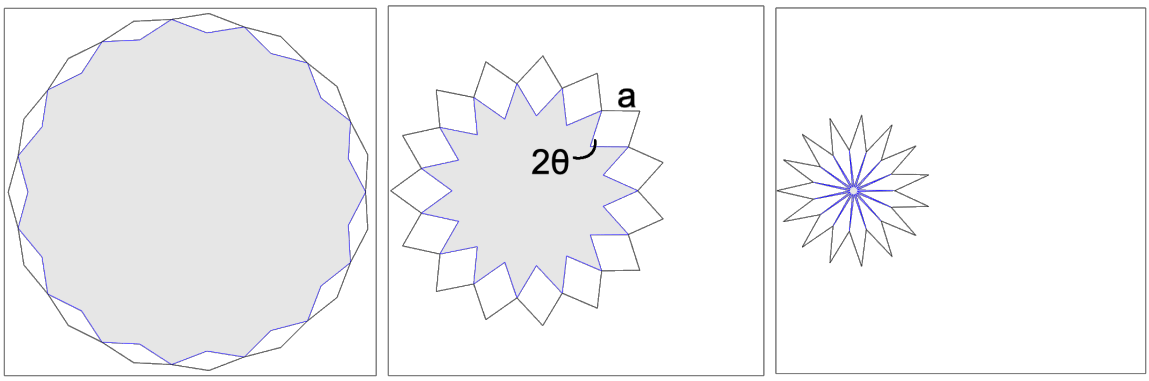

(a) Operation begins with the mechanism expanded.

(b) As the mechanism contracts the flux is compressed and the current and magnetic field increase.

(c) Finally, the mechanism has contracted completely and the current and magnetic field have reached a maximum.

Figure 6-2: Non-explosive Cylindrical Collapse Generator. The non-explosive cylindrical collapse FCG utilizes a Hoberman mechanism to contract radially. By running a current through the inner linkages (shown in blue), flux is trapped within the mechanism (in the gray area). One can then compress flux area by contracting the mechanism.

as the explosives used for typical, explosively-pumped FCGs tend to do.

Perhaps the greatest advantage provided by a non-explosive FCG is the potential for reusability. Deployable structures are designed for repeated use. Operating at lower speeds and without production of shock waves leads to less wear and tear on the system, providing potential for reuse. Rather than being single-shot devices, a non-explosive FCG could potentially be actuated in succession to provide a series of pulses.

The remaining two sections of this chapter give examples of this non-explosive FCG design strategy by using it to reimagine both the cylindrical implosion and the loop FCGs as non-explosive, employing the Hoberman mechanism.

6.2 Example — Non-explosive Cylindrical Collapse Generator

Figure 6-2 shows the operation of a Hoberman mechanism — a deployable structure that expands and contracts radially by employing a scissor mechanism, as seen in Figure 6-1. Figure 6-2a shows the mechanism nearly fully expanded, Figure 6-2b shows the mechanism mid-operation, and Figure 6-2c shows the mechanism nearly fully contracted. Since the mechanism has only this one degree of freedom, actuation can be controlled by linear motion of a single joint, assuming it behaves ideally under the stresses it experiences during flux compression. Actuation can therefore be provided by a number of means other than high explosives, such as gas expansion from depressurization or from lighting a propellant (which can more safely be experimented with in a lab setting and transported out of one than high explosives).

The proposed non-explosive cylindrical collapse FCG will be an extrusion of this mechanism out of the page, with current running through the inner linkages (shown in blue in Figure 6-2). The outer linkages would be insulating (shown in black). By running a current through the inner linkages, one can compress flux area (shaded gray in the figure) by contracting the mechanism. Operation begins with the mechanism expanded, as in Figure 6-2a. As the mechanism contracts, as in Figure 6-2b, the flux is compressed and the current and magnetic field increase. Finally, the mechanism has contracted completely, as in Figure 6-2c, and the current and magnetic field have reached a maximum.

For modeling by the methods of Chapter 3, one must calculate the perimeter of the conducting path and the flux area. In this case, the perimeter is a constant. Supposing each linkage has length a (as in Figure 6-2) and the mechanism is comprised by N rhombi ($N = 15$ in Figure 6-2), the perimeter is a constant $p = 2aN$. The area is slightly more complicated to calculate, and easiest expressed as a function of the angle 2θ shown in Figure 6-2. Through some simple geometry, one can show that the area is given by

$$A(\theta) = N \sin\left(\theta - \frac{\pi}{N}\right) \csc\left(\frac{\pi}{N}\right) \sin(\theta) a^2.$$

(a) Mechanism fully expanded (b) Mechanism partially contracted (c) Mechanism partially contracted

Figure 6-3: Custom hinges optimize for completeness of closure on contraction. CAD and mechanical design by Giselle Ventura and Daniel Lang of Draper.

The exact evolution of θ in time is highly dependent on the actuation mechanics, and so is here left unexamined.

While Figure 6-2 shows the operation of the mechanism with a single outer joint fixed, one could fix any point on the mechanism. Indeed, by using tracks along which certain joints may slide, one can fix the center point of the mechanism, if so desired. These tracks or a fixed inner joint provide a location for connection with the rest of the circuit — namely, the seed current source and a potential load coil. Unlike many explosively-pumped FCGs, there is nothing in this design that would automatically isolate the input after compression has begun, so care would have to be taken to do so, likely by means of a high power switch.

Rather than using traditional angulated scissors as in Hoberman's orginal patent [28] and in Figure 6-1, one could construct the mechanism using flexure joints, which would provide a more uniform conduction path. If angulated scissors are employed, conduction between linkages becomes a difficulty and a potential source of resistive losses, especially as a simple hinge-based design would require conduction through the hinge of the pin, which will typically provide an incomplete contact. Regardless of the implementation of the joints, flux compression will be limited by their ability to close completely.

Figure 6-3 shows a CAD of this design with custom hinges, optimizing for completeness of closure on contraction. When specifying dimensions for these generators,

one must give consideration not just to electromagnetic performance, but mechanical. For example, for optimal electromagnetic performance in a particular application, a tall generator might be desired, but in practice rapidly, stably, and reliably expanding and contracting a tall mechanism would present significant mechanical challenges.

Figure 6-3a shows the device at its most contracted, demonstrating the limited gain that would be possible with this implementation. Furthermore, the cost of fabrication for this particular design was prohibitive, so no experimental verification took place. Nevertheless, this simple design shows potential for a non-explosive version of the cylindrical implosion generator utilizing the Hoberman mechanism.

Another practical concern for these generators is conduction around the joints. If the joints are implemented with hinges, it is likely that conduction between plates only connected by the pin of the hinge will be necessary. Care must be taken that the pin and knuckle provide sufficient contact for conduction. If they do not, then they must be connected in a manner that does not interfere with (or at least does not prevent) motion, such as a conductive fluid filling the gap or a loose, elastic conductor connecting either the two knuckles directly or the knuckles to the pin, either externally or internally.

6.3 Example — Non-explosive Loop Generator

As another example, the proposed non-explosive loop FCG will be an extrusion of this mechanism out of the page, surrounded by an outer loop, with current running through the outer linkages and the outer loop (shown in blue in Figure 6-4). In this design, the inner linkages would be insulating (shown in black). By running a current through the outer linkages and the loop, flux is generated between the mechanism and the loop (in the gray area). One can compress flux area by expanding the mechanism. Operation begins with the mechanism contracted, as in Figure 6-4a. As the mechanism expands, as in Figure 6-4b, the flux is compressed and the current and magnetic field increase. Finally, the mechanism has expanded completely, as in Figure 6-4c, and the current and magnetic field have reached a maximum, as the area

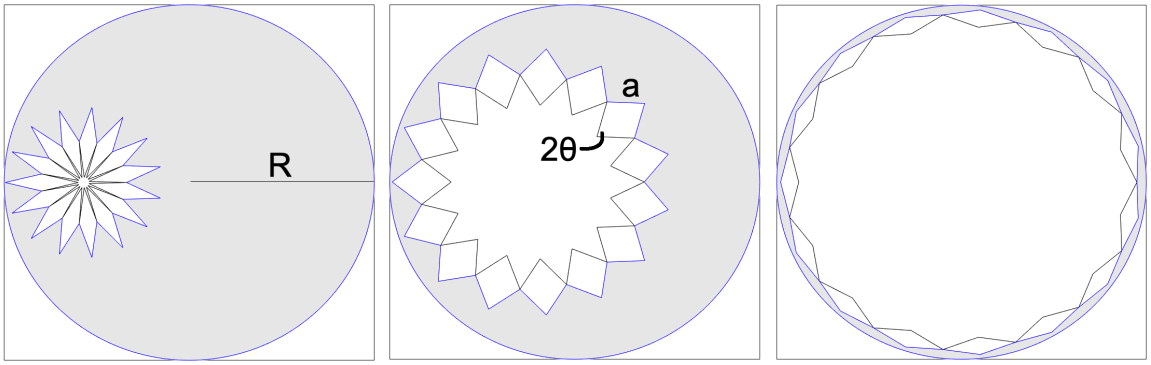

(a) Operation begins with the mechanism contracted.

(b) As the mechanism expands the flux between the mechansim and the loop is compressed and the current and magnetic field increase.

(c) Finally, the mechanism has expanded completely and the current and magnetic field have reached a maximum as the area between the mechanism and the loop has approached zero.

Figure 6-4: Non-explosive Loop Generator. The non-explosive loop FCG utilizes a Hoberman mechanism to expand and contracts radially within an outer loop. By running a current through the outer linkages and the outer loop (shown in blue), flux is stored between the mechanism and the loop (in the gray area). One can then compress flux area by expanding the mechanism.

between the mechanism and the loop has reached a minimum.

For modeling by the methods of Chapter 3, one must calculate the perimeter of the conducting path and the flux area of this new geometry. Once again, the perimeter is a constant. With the same parameterization as the cylindrical collapse generator, and letting the radius of the loop be R (as in Figure 6-4), the perimeter is a constant $p = 2\pi R + 2aN$. Through some simple geometry, one can show that the area is given by

$$A(\theta) = \pi R^2 - N \sin(\theta) \csc\left(\frac{\pi}{N}\right) \sin\left(\theta + \frac{\pi}{N}\right) a^2.$$

Once more, the time-evolution of θ is actuation-method-dependent.

In this design as well, one could fix any point on the mechanism, however, since the outer linkages must make contact with the loop, the simplest design would be to fix an outer joint, attached to the loop. Like the non-explosive cylindrical collapse generator before it, this generator does not automatically seal off the input, so this must be done separately. The loop in this topology provides ample opportunity to

connect a seed current source and any potential load coil in the same manner pictured in Chapter 2, Figure 6-4 for the explosively-pumped loop generator. Since the hinges limit expansion less than they limit collapse (as demonstrated in Figure 6-3), the loop topology shows more promise for high gain in real implementations than the cylindrical collapse generator. Note that in the ideal case — wherein the Hoberman mechanism can open and close completely — the loop generator would have less gain, since there would remain space between the loop and the mechanism in the loop generator, but there would be no space left in the cavity of the ideal cylindrical collapse generator.

6.4 Summary and Conclusions

This chapter proposes a means of translating existing explosively-pumped FCG designs into non-explosive FCG designs by replacing conductors that deform under the force of an explosion with deployable structures that can perform the same deformation of the conducting path (and consequent compression of flux area) without destroying the generator. Not only does this provide safety advantages by removing the need for high explosives, but also potential efficiency gains by not wasting energy in the deformation of the metal and potential for reuse of a single generator system. Beyond just theoretically proposing this new class of non-explosive FCGs, this chapter presents two examples, based on the cylindrical implosion and loop generators. This class of generators, and these two designs in particular, require experimental and numerical verification to more fully evaluate advantages and disadvantages of this approach.

Chapter 7

Summary, Conclusions, and Further Work

This thesis has surveyed, modeled, and presented designs of flux compression generators. This chapter summarizes the thesis as well as providing conclusions and suggestions for further work. It is organized linearly by chapter (placing the Appendix within the body where it most naturally fits), addressing each chapter in turn and highlighting connections between chapters.

In Chapter 2, general FCG operation was described, largely qualitatively. This author found it to be more effective for understanding the operation of both general FCGs and any particular FCG to survey various FCG topologies, considering their operation and comparing them with each other to gain a more intuitive understanding of flux compression, rather than studying one design deeply. For this survey, the plate, cylindrical implosion, loop, strip, coaxial, disk, and helical generators were chosen and particularly arranged to highlight similarities between topologies. Indeed, this review is not intended to be a resource for deciding between these generator topologies for any given application or list of requirements (for this purpose, see the resources referenced in compiling this chapter), but rather an introduction for someone with little-to-no experience with FCGs to understand the general operating principles of flux compression generators by highlighting the structural similarities and differences of these generators and their mechanism of flux compression.

Chapter 3 contains a new model for flux compression generators in the shape of a generalized cylinder, such as the plate generator, the cylindrical implosion generator, the loop generator, and the strip generator — all reviewed in Chapter 2. The primary feature of this model, differentiating it from the often-used circuit models, is its more rigorous treatment of the effects of magnetic diffusion. Circuit models primarily ignore magnetic diffusion or use a linear approximation for the skin depth. The model presented in Chapter 3 provides an intermediary between such simplistic approximations and outright calculation of the fields throughout the entire generator, which is different for every geometry and will often require finite-element analysis. (To provide a bridge between the field-based model of this chapter and the circuit model often more directly useful in pulsed-power, the Appendix provides a new means of calculating the inductance of the same FCG geometry considered in Chapter 3. Included in this manner of inductance calculation is a formulation in terms of partial inductances. The inductance of all generators both mentioned in Chapter 2 and in the form considered in Chapter 3 could be calculated directly from the partial self- and mutual-inductances of rectangular and curved plates, i.e., extrusions of line segments and circular arcs. Some such calculations could be done analytically.) By more thoroughly treating magnetic diffusion, not only can the model more accurately predict the dynamics of systems heavily impacted by magnetic diffusion, but also whether any given system is likely to be limited by diffusion or if inefficiencies in a realized system compared to equivalent circuit models are due to other sources of flux loss.

The largest source of error in the treatment of magnetic diffusion in the model of Chapter 3 is likely the truncation of infinite Fourier series to only a single term. In future efforts, one could truncate fewer terms from the series (resulting in a higher-order DAE) and provide an analysis of the effects of truncation.

Additionally, the model and its assumptions and approximations should be verified by comparing expected results with more experimental data. One feature of the increased emphasis on magnetic diffusion is a more accurate treatment of low speed experiments, when magnetic diffusion is more likely to dominate, so experimental verification should also be done with low-speed tests (if it proves impossible to do a

low-speed explosive test, verification can be accomplished with non-explosive FCG designs from Chapter 6).

Furthermore, the model of Chapter 3 assumes the width of the expanding or contracting conductor to remain constant, but in reality conservation of mass requires the thickness to decrease or increase, respectively, to maintain a constant density. A function for the thickness in terms of the geometric state variables is generally a simple matter, but thorough treatment of the changing width requires solving a diffusion boundary-value problem with a moving boundary condition. It is likely also possible to bound the effect of the varying thickness and make an approximation from there. This author has not come across a treatment of the effect of the changing conductor thickness in existing literature.

Finally, in the case of unloaded FCGs, the model lacks definition of a clear stopping point. Turnaround has been observed in some generators, but in cases that it is preceded by mechanical failure there is currently no means of determining the point of failure, which in turn determines the maximum magnetic field and current. This useful addition to the model would likely only come from future experimental research.

Chapter 3 also examines the cylindrical implosion generator and the loop generator with the aforementioned model. These simulations — particularly the cylindrical implosion generator, in which turnaround is expected at times — would also benefit from a greater consideration of the mechanics involved in the elasto-plastic deformation of the metal so as to better predict the turnaround radius and reap greater benefits from the inclusion of magnetic pressure. Such considerations are less necessary for the loop generator, in which such effects are unlikely to have great impact before mechanical failure.

Section 3.7 revealed that the magnetic field measured in the near-field, but far enough away that the generator seems small, is unaffected by flux compression. This little-mentioned fact has bearings in applications, as it implies FCGs cannot be used for direct field generation outside of the generator — they must have a load coil for this purpose. This result also allows for a more direct measurement of flux in the device, as shown in Chapter 5, and prevents indirect measurement of the field within

the cavity by a sensor farther than verging on inside the cavity.

The initial current source was considered in Chapter 4. First, a design was provided for a capacitor bank source. Should simulation or experiment show that the pulse is too long-lasting and magnetic forces are likely to cause mechanical failure prior to detonation, one might consider modifying the capacitor bank into a Marx generator, which is capable of providing a faster seed-current pulse. Additionally, a current sensor could be added to the bank to ensure detonation only occurs once the current has reached its optimal value.

Perhaps most importantly, it was seen that a single capacitor of this six-capacitor bank is comparable in size to — even larger than — the generator designed in Chapter 5, and so is a poor choice for miniaturization. For effective miniaturization of the full system, a ferromagnetic generator or ferroelectric generator is likely necessary to provide the seed current.

In Chapter 5, a loop generator design was presented. Design parameters are presented in Table 5.1 were found by trial and error using the model developed in Chapter 3, optimizing for magnetic field strength within the cavity, constrained by the size of the generator and availability of copper pipes of such dimensions. Future efforts could give insights to the effect of variations in loop radius, shell radius, thickness, and separation between loop and shell centers. Of great import to future designs is not only the direction of such effect, but also the sensitivity of current and magnetic field strength to changes in such parameters, which influences not only chosen values, but also fabrication tolerances.

Also in Chapter 5 was a description of an experiment that can be run to test/characterize an FCG, particularly optimized for the design presented earlier in the same chapter. Section 3.7 showed that measurement of the effects of flux compression must occur within or very close to the cavity of the generator, as there is no effect at a distance, since the field away from the generator depends on the flux within the cavity, not the field strength in the cavity. Following these insights, two magnetometers were designed — one for placement very near to the device so as to capture the magnetic field within the generator without destruction prior to

data capture, and one for placement far enough from the generator as to capture a magnetic field proportional to the flux within the generator. The timing of the pulse is such that radio frequency components are not necessary, but the system is reaching the upper bandwidth limit of standard components, so care must be taken when selecting parts for these magnetometers to ensure the signal remains undistorted.

Another insight that might be gained from running the experiment of Chapter 5 would be to characterize the decay of the effects of flux compression. Maxwell's equations dictate a smooth transition between the area-dependent magnetic field within the generator and the area-independent magnetic field once the generator can be seen as a dipole, but this transition is difficult to simulate and predict. Experimental characterization by setting multiple magnetometers at increasing distances from the generator could aid in better understanding this effect.

Finally, Chapter 6 presented a new class of non-explosive FCGs that utilize deployable structures to substitute high-speed, explosive deformation of conductors. Since these generators operate at lower speeds, magnetic diffusion is a greater contributor to their losses, so the model developed in Chapter 3 becomes an asset in their numerical evaluation and should be employed. These generators require experimental verification in addition to numerical — particularly the two designs presented that utilize the Hoberman mechanism.

Because FCGs of this class do not rely on irreversible deformations of metal, they hold potential to be reused. Once a single-use generator of this class has been fabricated and experimentally verified, efforts should be made to demonstrate reusability. Despite operating at lower speeds than their explosive counterparts, care must be taken to slow these generators as they reach peak compression, so as to not destroy themselves, ruining any chance of reusability. The most natural manner for doing so is perhaps to ensure that magnetic pressure is high enough to prevent a catastrophic collision, rather cushioning the impact. Of equal importance to reusability of the system is the ability of the seed-current source to be reused. Despite capacitor banks being larger than FMGs and FEGs, they are more readily adapted for repeated use.

The results of this thesis are new models and designs for existing and novel flux

compression generators, as well as current sources to power them and experiments to verify their operation. Particular emphasis was placed the loop generator, which is currently underserved by literature, especially given its suitability for the increasingly common "minigen" design constraints. Hopefully these models and designs enable increased innovation in flux compression generators and allow for their application to new and exciting pulsed-power applications.

7.1 Suggestions for Future Work

These suggestions are provided in context in the preceding section, but are collected here for the convenience of the reader.

While one goal in developing the model presented in Chapter 3 was simplicity and ease of use, it can still be expanded and improved while maintaining the advantages of a low order DAE model. Such modifications include reevaluation of the assumption of a constant width and varying density of the conductor, likely suggesting the allowance of a varying width (instead or perhaps in addition to a varying density); the prediction of a failure point in the case of unloaded generators; and greater consideration of the mechanical dynamics of the conductor, particularly with regard to its elasto-plastic deformation. With or without these modifications, the model also requires experimental verification, particularly with topologies and at speeds where the effects of magnetic diffusion are expected to be prominent. It is for this reason that the experimental set-up of Chapter 5 was provided and should be run.

Other insights that might be gained by experimental verification include the effects of variations in loop radius, shell radius, thickness, and separation between loop and shell centers. Additionally, efforts should be made to experimentally and (numerically, through finite element analysis) characterize the decay of the effects of flux compression, which section 3.7 showed cannot be observed at even a moderate distance from the generator.

Finally, the theoretical designs put forward in Chapter 6 require experimental and numerical verification. This class of generators should be examined for potential as

a reusable flux compression generator.

Appendix A

Inductance of an Extrusion of a Planar Curve

A reliable inductance model forms the basis of translation from a field-based perspective to a current-based perspective of the dynamics of a flux compression generator (FCG) (see Chapter 3). Means of calculating both magnetic field intensity and current are essential, as applications vary between primarily generating a large current pulse and primarily generating a high intensity magnetic field. This can be easily achieved using the inductance of the generator as the flux can be expressed as $\lambda = Li$, where L is the inductance and i is the current or as $\lambda = BA$, where B is the average field and A is the area, so the current is related to the field by $i = \frac{A}{L}B$. In this chapter, we develop a means of calculating the inductance of the extrusion of a planar curve (i.e., a generalized right cylinder), assuming the currents flow along the surface (as the effects of diffusion were considered separately in Chapter 3). This general form describes the geometry of a number of the FCG topologies reviewed in Chapter 2, i.e., plate, cylindrical implosion, loop, and strip. We demonstrate agreement in the limiting case between the formula developed here and the Neumann formula for self-inductance of a current loop. We also give special consideration to the case of a planar curve that is most naturally broken into segments, applying the concept of partial inductance.

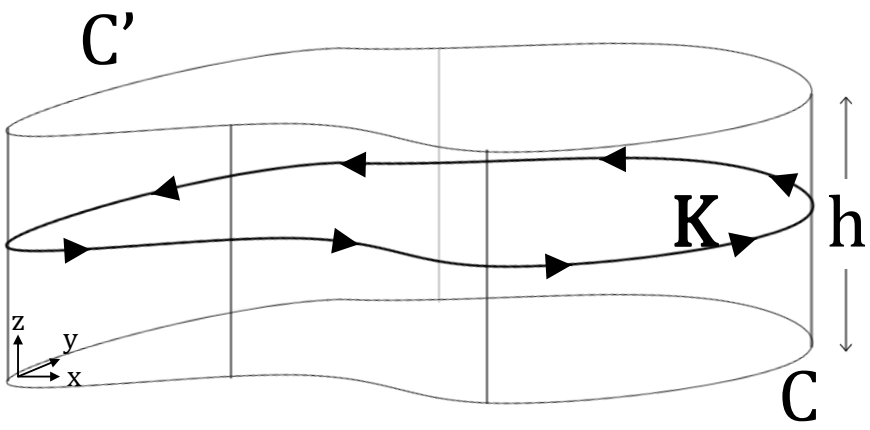

Figure A-1: Extrusion of the planar curve C into the 3D surface S of height h. Surface current density $\mathbf{K}$ flows around S parallel to the x-y plane.

A.1 Inductance of Extrusion

All FCGs that can be modeled in the manner developed in Chapter 3 can be constructed by extruding a planar curve, C, along a line segment perpendicular to the plane in which C resides (pictured in Figure A-1). Extrusion yields a perfectly conducting surface, S, in 3D space with height h. Each cross section of S parallel to the base is congruent to C. Without loss of generality, let C (and therefore the base) reside in the x-y plane and the extrusion occur in the $+\hat{z}$ direction, such that the curve C' in the figure resides in the $z = h$ plane.

Suppose there is a surface current flowing around the surface (along C in each cross section parallel to the x-y plane) with uniform surface current density magnitude $K = \frac{i}{h}$. Let the inductance, L, be defined by the potential energy, U, and the relation

$$U = \frac{1}{2}Li^2. \tag{A.1}$$

We can calculate the potential energy from the formula

$$U = \frac{1}{2}\iiint_V \mathbf{J} \cdot \mathbf{A} dv, \tag{A.2}$$

which, in the limit of an infinintely-thin volume becoming a surface, is equivalent to

$$U = \frac{1}{2} \iint_S \mathbf{K} \cdot \mathbf{A} da, \tag{A.3}$$

where $\mathbf{A}$ is the magnetic vector potential ($\mathbf{B} = \nabla \times \mathbf{A}$), $\mathbf{J}$ is the current density, and $\mathbf{K}$ is the surface current density.

Assuming magnetoquasistatics, decaying fields at infinity, and a lack of nearby conductors, the magnetic vector potential at a point $\mathbf{r}$ is given by the superposition integral

$$\mathbf{A}(\mathbf{r}) = \frac{\mu_0}{4\pi} \iiint_{\mathbf{r}' \in V} \frac{\mathbf{J}(\mathbf{r}')}{\|\mathbf{r} - \mathbf{r}'\|} dv', \tag{A.4}$$

which becomes

$$\mathbf{A}(\mathbf{r}) = \frac{\mu_0}{4\pi} \iint_{\mathbf{r}' \in S} \frac{\mathbf{K}(\mathbf{r}')}{\|\mathbf{r} - \mathbf{r}'\|} da', \tag{A.5}$$

in our surface-current limit.

Rewriting each double integral as a line integral around C and an integral over the height and substituting in the surface current, we have

$$U = \frac{1}{2} \oint_C \int_0^h \frac{i}{h} \hat{\mathbf{s}} \cdot \mathbf{A}(\mathbf{s} + z\hat{\mathbf{z}}) \, dz \, ds \tag{A.6}$$

and

$$\mathbf{A}(\mathbf{r}) = \frac{\mu_0}{4\pi} \oint_C \int_0^h \frac{\frac{i}{h}\hat{\mathbf{s}}}{\|\mathbf{r} - (\mathbf{s} + z\hat{\mathbf{z}})\|} \, dz \, ds, \tag{A.7}$$

where the line integrals are around C and parameterized by $\mathbf{s} = (s_x, s_y, 0)$, the unit vector of which is $\hat{\mathbf{s}}$.

Substituting eq. (A.7) into eq. (A.6) gives the following equation for the potential energy,

$$U = \frac{1}{2} i^2 \oint_C \frac{1}{h} \int_0^h \frac{\mu_0}{4\pi} \oint_C \frac{1}{h} \int_0^h \frac{\hat{\mathbf{s}} \cdot \hat{\mathbf{s}}'}{\|(\mathbf{s}' + z'\mathbf{z}) - (\mathbf{s} + z\hat{\mathbf{z}})\|} \, dz' \, ds' \, dz \, ds. \tag{A.8}$$

From the definition of inductance (eq. (A.1)), we now have a quadruple-integral

formula for the inductance that depends only on the geometry of the device,

$$L = \frac{\mu_0}{4\pi} \oint_C \oint_C \hat{\mathbf{s}} \cdot \hat{\mathbf{s}}' \frac{1}{h} \int_0^h \frac{1}{h} \int_0^h \frac{1}{\|(\mathbf{s}' - \mathbf{s}) + (z' - z)\hat{\mathbf{z}}\|} \, dz' \, dz \, ds' \, ds. \tag{A.9}$$

Let us consider the inner double integral,

$$I = \frac{1}{h} \int_0^h \frac{1}{h} \int_0^h \frac{1}{\|(\mathbf{s} - \mathbf{s}') + (z - z')\hat{\mathbf{z}}\|} \, dz' \, dz. \tag{A.10}$$

Noting that the integrand only depends on the difference between z and z', we substitute $\Delta z = z - z'$ into the integral to get

$$I = \frac{1}{h} \int_0^h \frac{1}{h} \int_{z-h}^{z} \frac{1}{\|(\mathbf{s} - \mathbf{s}') + \Delta z\hat{\mathbf{z}}\|} \, d(\Delta z) \, dz, \tag{A.11}$$

which we can split into two separate integrals,

$$I = \frac{1}{h} \int_0^h \frac{1}{h} \int_0^z \frac{1}{\|(\mathbf{s} - \mathbf{s}') + \Delta z\hat{\mathbf{z}}\|} \, d(\Delta z) \, dz + \frac{1}{h} \int_0^h \frac{1}{h} \int_{z-h}^{0} \frac{1}{\|(\mathbf{s} - \mathbf{s}') + \Delta z\hat{\mathbf{z}}\|} \, d(\Delta z) \, dz. \tag{A.12}$$

Swapping the order of integration of both integrals gives

$$I = \frac{1}{h} \int_0^h \frac{1}{h} \int_{\Delta z}^{h} \frac{1}{\|(\mathbf{s} - \mathbf{s}') + \Delta z\hat{\mathbf{z}}\|} \, dz \, d(\Delta z) + \frac{1}{h} \int_{-h}^{0} \frac{1}{h} \int_0^{\Delta z + h} \frac{1}{\|(\mathbf{s} - \mathbf{s}') + \Delta z\hat{\mathbf{z}}\|} \, dz \, d(\Delta z). \tag{A.13}$$

Since the integrands are constant with respect to the inner integration variable, z, the inner integrals become multiplication by the difference of their bounds, so

$$I = \frac{1}{h^2} \int_0^h \frac{h - \Delta z}{\|(\mathbf{s} - \mathbf{s}') + \Delta z\hat{\mathbf{z}}\|} \, d(\Delta z) + \frac{1}{h^2} \int_{-h}^{0} \frac{h + \Delta z}{\|(\mathbf{s} - \mathbf{s}') + \Delta z\hat{\mathbf{z}}\|} \, d(\Delta z). \tag{A.14}$$

At this point, we can return I to a single integral, rather than a summation of integrals,

$$I = \frac{1}{h^2} \int_{-h}^{h} \frac{h - |\Delta z|}{\|(\mathbf{s} - \mathbf{s}') + \Delta z\hat{\mathbf{z}}\|} \, d(\Delta z). \tag{A.15}$$

Using the facts that the integrand is even, the bounds are negations of each other,

and $(\mathbf{s}-\mathbf{s}') \perp \hat{\mathbf{z}}$,

$$I = \frac{2}{h^2}\int_0^h \frac{h-\Delta z}{\sqrt{\|\mathbf{s}-\mathbf{s}'\|^2+(\Delta z)^2}}\, d(\Delta z). \tag{A.16}$$

Evaluating this integral gives

$$I = \frac{2}{h}\left(\log\left(\left(\Delta z + \sqrt{\|\mathbf{s}-\mathbf{s}'\|^2+\Delta z^2}\right)/h\right) - \sqrt{\|\mathbf{s}-\mathbf{s}'\|^2+\Delta z^2}/h\right)\Bigg|_0^h \tag{A.17}$$

$$= \frac{2}{h}\left(\log\left(\frac{h}{\|\mathbf{s}-\mathbf{s}'\|}+\sqrt{1+\frac{h^2}{\|\mathbf{s}-\mathbf{s}'\|^2}}\right) - \frac{h}{\|\mathbf{s}-\mathbf{s}'\|+\sqrt{h^2+\|\mathbf{s}-\mathbf{s}'\|^2}}\right) \tag{A.18}$$

Substituting back into eq. (A.9), the inductance is therefore given by

$$L = \frac{\mu_0}{2\pi h}\oint_C\oint_C \hat{\mathbf{s}}\cdot\hat{\mathbf{s}}'\left(\log\left(\frac{h}{\|\mathbf{s}-\mathbf{s}'\|}+\sqrt{1+\frac{h^2}{\|\mathbf{s}-\mathbf{s}'\|^2}}\right) - \frac{h}{\|\mathbf{s}-\mathbf{s}'\|+\sqrt{\|\mathbf{s}-\mathbf{s}'\|^2+h^2}}\right) ds'\, ds. \tag{A.19}$$

In this form, the effects of the finite height of the inductor have been completely accounted for in the integrand and the integration only occurs over the curve, considering the contribution of inductance from linkage between vertical strips at two positions (s and s') coming off the curve C.

A.2 Agreement with Neumann Formula

As a brief means of verification of the preceding inductance formula (eq. (A.19)), we consider the limiting case of $h \to 0$, in which case we are considering the inductance of an arbitrary planar current loop along a thin wire.

First, note that the integrand evaluates to 0 when $h = 0$. We can then consider L as taking the form

$$L = \frac{f(h)}{h} = \frac{f(h)-f(0)}{h-0}. \tag{A.20}$$

From the definition of the derivative, we have

$$\lim_{h\to 0} L = \lim_{h\to 0} \frac{f(h) - f(0)}{h - 0} = f'(0). \tag{A.21}$$

Since the paths of integration are independent of h, it suffices to differentiate the integrand with respect to h,

$$\frac{d}{dh}\left[\log\left(\frac{h}{\|\mathbf{s}-\mathbf{s}'\|} + \sqrt{1+\frac{h^2}{\|\mathbf{s}-\mathbf{s}'\|^2}}\right) - \frac{h}{\|\mathbf{s}-\mathbf{s}'\| + \sqrt{h^2+\|\mathbf{s}-\mathbf{s}'\|^2}}\right]\Bigg|_{h=0} \tag{A.22}$$

$$= \frac{1}{\sqrt{h^2+\|\mathbf{s}-\mathbf{s}'\|^2}} - \frac{\|\mathbf{s}-\mathbf{s}'\| + \sqrt{h^2+\|\mathbf{s}-\mathbf{s}'\|^2} - \frac{h^2}{\sqrt{h^2+\|\mathbf{s}-\mathbf{s}'\|^2}}}{\left(\|\mathbf{s}-\mathbf{s}'\| + \sqrt{h^2+\|\mathbf{s}-\mathbf{s}'\|^2}\right)^2}\Bigg|_{h=0}$$

$$= \frac{1}{\|\mathbf{s}-\mathbf{s}'\|} - \frac{2\|\mathbf{s}-\mathbf{s}'\|}{(2\|\mathbf{s}-\mathbf{s}'\|)^2} \tag{A.23}$$

$$= \frac{1}{2\|\mathbf{s}-\mathbf{s}'\|}. \tag{A.24}$$

So, the inductance would be given by

$$L = \frac{\mu_0}{4\pi}\oint_C \oint_{C^*} \frac{\hat{\mathbf{s}}\cdot\hat{\mathbf{s}}'}{\|\mathbf{s}-\mathbf{s}'\|}\, ds'\, ds, \tag{A.25}$$

where C is along the surface of the wire, as before, and C^* is along the center of the wire. The modification from C to C^* is necessary for the convergence of this integral; if both integrations occurred over C, the integral would diverge, a consequence of the faulty assumption of an infintesimal wire. This inductance formula matches Neumann's self-inductance formula in [30, p.147]. Other corrections to solve the convergence problem have been suggested that leave the paths of integration in place, but leave out the problematic segment when the two curves overlap and the integrand explodes [31]. Another possible option in the case of planar wire loops, rather than correcting the Neumann formula by shifting the contour of integration, would be to consider a thin wire to be equivalent to an infinitesimally thin ribbon with height equal to the diameter of the wire and evaluate the here-derived extrusion inductance

formula, setting h to the diameter of the wire. This formula does not suffer the same trouble with a divergent integral, as the singularity occurs whenever $\mathbf{s}$ approaches $\mathbf{s}'$, which prevents integration in the case of a wire loop (in which case the integral diverges just as $\int_0^1 \frac{1}{x} dx$ diverges), but in the case of an extrusion, the integral is now in the form of $\int_0^1 \log(\frac{1}{x}) dx$, which does converge.

A.3 Partial Inductance of a Segmented Extrusion

In some cases, the curve C will most naturally be considered a combination of N segments, $\{C_n\}_{n=1}^N$. Each segment, C_n, is then extruded into a surface segment, S_n, which combined form the surface, S, mentioned previously. Along the surface segment, S_n, flows current density $\mathbf{K}_n$ such that $\|\mathbf{K}_n\| = \frac{i_n}{h}$. Assuming no charges build up at the interface between segments (a vital assumption in magnetoquasistatics), $i_n = i$ for all $n \in \{1 \dots N\}$. For such cases, it is useful to consider individually the contribution of each segment to the inductance.

We can break up the surface integral for potential energy to integrate over the surface segments,

$$U = \frac{1}{2} \sum_{n=1}^{N} \iint_{S_n} \mathbf{K}_n \cdot \mathbf{A} da. \tag{A.26}$$

The magnetic vector potential can be similarly broken up,

$$\mathbf{A}(\mathbf{r}) = \frac{\mu_0}{4\pi} \sum_{m=1}^{N} \iint_{\mathbf{r}' \in S_m} \frac{\mathbf{K}_m(\mathbf{r}')}{\|\mathbf{r} - \mathbf{r}'\|} da'. \tag{A.27}$$

Just as before, we can consider these surface integrals as the integral of a line integral

and combine the two equations, so

$$U = \frac{1}{2}\sum_{n=1}^{N} i_n \int_{C_n} \frac{1}{h}\int_0^h \frac{\mu_0}{4\pi}\sum_{m=1}^{N} i_m \int_{C_m} \frac{1}{h}\int_0^h \frac{\hat{\mathbf{s}}_n \cdot \hat{\mathbf{s}}_m}{\sqrt{\|\mathbf{s}_n - \mathbf{s}_m\|^2 + (z_n - z_m)^2}}\, dz_m\, ds_m\, dz_n\, ds_n \tag{A.28}$$

$$= \frac{1}{2}\sum_{n=1}^{N} i_n^2 \int_{C_n} \frac{1}{h}\int_0^h \frac{\mu_0}{4\pi}\int_{C_n} \frac{1}{h}\int_0^h \frac{\hat{\mathbf{s}} \cdot \hat{\mathbf{s}}'}{\sqrt{\|\mathbf{s} - \mathbf{s}'\|^2 + (z - z')^2}}\, dz'\, ds'\, dz\, ds$$
$$+ \frac{1}{2}\sum_{n=1}^{N}\sum_{m\neq n} i_m i_n \int_{C_n} \frac{1}{h}\int_0^h \frac{\mu_0}{4\pi}\int_{C_m} \frac{1}{h}\int_0^h \frac{\hat{\mathbf{s}}_n \cdot \hat{\mathbf{s}}_m}{\sqrt{\|\mathbf{s}_n - \mathbf{s}_m\|^2 + (z_n - z_m)^2}}\, dz_m\, ds_m\, dz_n\, ds_n. \tag{A.29}$$

We can now define the partial self-inductance, L_n, of each surface S_n and its partial mutual inductance, M_{mn}, with each other surface S_m as

$$L_n = \frac{\mu_0}{4\pi}\int_{C_n} \frac{1}{h}\int_0^h \int_{C_n} \frac{1}{h}\int_0^h \frac{\hat{\mathbf{s}} \cdot \hat{\mathbf{s}}'}{\sqrt{\|\mathbf{s} - \mathbf{s}'\|^2 + (z - z')^2}}\, dz'\, ds'\, dz\, ds \tag{A.30}$$

and

$$M_{mn} = \frac{\mu_0}{4\pi}\int_{C_n} \frac{1}{h}\int_0^h \int_{C_m} \frac{1}{h}\int_0^h \frac{\hat{\mathbf{s}}_n \cdot \hat{\mathbf{s}}_m}{\sqrt{\|\mathbf{s}_n - \mathbf{s}_m\|^2 + (z_n - z_m)^2}}\, dz_m\, ds_m\, dz_n\, ds_n, \tag{A.31}$$

such that

$$U = \frac{1}{2}\sum_{n=1}^{N} L_n i_n^2 + \sum_{n=1}^{N}\sum_{m>n} M_{mn} i_m i_n, \tag{A.32}$$

since $M_{mn} = M_{nm}$, as is to be expected of partial mutual inductance. Considering that $i_n = i$ for all n, this expression for the potential energy also yields an expression for the total self-inductance in terms of these partial self-inductances and partial mutual inductances,

$$L = \sum_{n=1}^{N} L_n + 2\sum_{n=1}^{N}\sum_{m>n} M_{mn}. \tag{A.33}$$

These expressions can be simplified in the same manner as the expression for the

self-inductance of the loop, yielding

$$L_n = \frac{\mu_0}{2\pi h}\int_{C_n}\int_{C_n} \hat{\mathbf{s}}\cdot\hat{\mathbf{s}}'\left(\log\left(\frac{h}{\|\mathbf{s}-\mathbf{s}'\|}+\sqrt{1+\frac{h^2}{\|\mathbf{s}-\mathbf{s}'\|^2}}\right)-\frac{h}{\|\mathbf{s}-\mathbf{s}'\|+\sqrt{h^2+\|\mathbf{s}-\mathbf{s}'\|^2}}\right)ds'\,ds, \quad \text{(A.34)}$$

and

$$M_{mn} = \frac{\mu_0}{2\pi h}\int_{C_n}\int_{C_m} \hat{\mathbf{s}}_n\cdot\hat{\mathbf{s}}_m\left(\log\left(\frac{h}{\|\mathbf{s}_n-\mathbf{s}_m\|}+\sqrt{1+\frac{h^2}{\|\mathbf{s}_n-\mathbf{s}_m\|^2}}\right)-\frac{h}{\|\mathbf{s}_n-\mathbf{s}_m\|+\sqrt{h^2+\|\mathbf{s}_n-\mathbf{s}_m\|^2}}\right)ds_m\,ds_n. \quad \text{(A.35)}$$

At this point, it is worth noting the distinction between these partial self- and mutual-inductances and the usual loop self- and mutual-inductances. Comparing our equation for the self-inductance of an extruded loop and an extruded segment, we see that the only difference lies in the path of the line integral. In the case of the loop, the line integral is along a closed curve, which is not the case for the extruded segment. If we were to attempt to consider the inductance of an extruded segment in isolation, we would be tempted to go through the same steps as previously, yielding the same equation we have here, but in truth we would not make it past the second step of the derivation when we assume a quasistatic regime and therefore no charge buildup. With no return path for the current and no charge buildup, the continuity equation is violated. From another perspective, the lack of a return path leaves the flux area being considered undefined, which leaves inductance (a measure of flux linkage from a given current) undefined. For a physical interpretation, we must specify a return path.

Considering the extrusion of a straight segment (i.e., a rectangle rather than a curved surface), a physical interpretation may be derived from the volume formed by drawing the rectangle again at infinity and connecting the two into a right rectangular prism. If we consider the contribution of our original rectangle to the self-inductance

of this new inductor, we see that the perpendicular surfaces do not contribute, since the vector potential is perpendicular to the current. The surface at infinity also offers no contribution, since the vector potential has died off at infinity. So the only contribution comes from the original rectangle; this is the partial self-inductance of this rectangle, a fundamental property of the rectangle, regardless of return path [30]. Mutual self-inductance has a similar physical interpretation by considering the flux linkage between two parallel rectangles. Such physical interpretations become more difficult to provide for curved surfaces and arbitrary relative positioning, but perhaps more important is the mathematical definition given above.

Bibliography

[1] C. M. Fowler and L. L. Altgilbers, "PACS №: 84.70+p magnetic flux compression generators: A tutorial and survey contents," Los Alamos National Lab, 2003. [Online]. Available: https://pdfs.semanticscholar.org/f20b/94c86b9620166bdb82556b5be93261c80c64.pdf.

[2] E. W. Lee, "Megagauss physics and technology," *Physics Bulletin*, vol. 32, no. 4, pp. 110–111, Apr. 1981. DOI: 10.1088/0031-9112/32/4/030.

[3] B. Novac, M. Istenic, J. Luo, I. Smit, J. Brown, M. Hubbard, P. Appelgren, M. Elfsberg, T. Hurtig, C. Nylander, A. Larsson, and S. Nyholm, "A 10 GW pulsed power supply for HPM sources," *IEEE Transactions on Plasma Science*, vol. 34, no. 5, pp. 4–4, 2006. [Online]. Available: https://ieeexplore.ieee.org/abstract/document/1710045.

[4] P. Bartkowski and P. Berning, "Design and testing of the ARL squeeze 4 helical flux compression generator," 2013.

[5] M. A. Elsayed, A. A. Neuber, J. C. Dickens, J. W. Walter, M. Kristiansen, and L. L. Altgilbers, "An explosively driven high-power microwave pulsed power system," *Review of Scientific Instruments*, vol. 83, no. 2, 2012. DOI: 10.1063/1.3681443.

[6] P. Appelgren, G. Bjarnholt, N. Brenning, M. Elfsberg, T. Hurtig, A. Larsson, B. M. Novac, and S. E. Nyholm, "Small helical magnetic flux-compression generators: Experiments and analysis," *IEEE Transactions on Plasma Science*, vol. 36, no. 5, pp. 2673–2683, 2008. DOI: 10.1109/TPS.2008.2003966.

[7] L. Altgilbers, "Recent advances in explosive pulsed power," U.S. Army Space and Missile Defense Command, Huntsville, AL, 35748, PACS №: 84.70+p, 2003, p. 24. [Online]. Available: https://pdfs.semanticscholar.org/af5a/ad777e9648aacac50673b9961be3557fa0a0.pdf?_ga=2.118092875.353175796.1574549089-1334257001.1563762085.

[8] J. E. Gover, O. M. Stuetzer, and J. L. Johnson, "Small helical flux compression amplifiers," in *Megagauss Physics and Technology*, Springer US, 1980, pp. 163–180. DOI: 10.1007/978-1-4684-1048-8_15.

[9] P. Appelgren, N. Brenning, T. Hurtig, A. Larsson, B. M. Novac, and S. E. Nyholm, "Modeling of a small helical magnetic flux-compression generator," *IEEE Transactions on Plasma Science*, vol. 36, no. 5, pp. 2662–2672, 2008. DOI: 10.1109/TPS.2008.2003077.

[10] A. S. Dickson, "Theoretical study of flux compression for the conceptual design of a non-explosive FCG," MSc - Electrical and Information Engineering, University of the Witwatersrand, Johannesburg, Johannesburg, South Africa, Oct. 31, 2006, 114 pp. [Online]. Available: http://wiredspace.wits.ac.za/handle/10539/1521.

[11] H. Knoepfel, *Pulsed high magnetic fields: physical effects and generation methods concerning pulsed fields up to the megaoersted level*. North-Holland, 1970.

[12] L. L. Altgilbers, I. Grishnaev, I. R. Smith, Y. Tkach, M. D. J. Brown, B. M. Novac, and I. Tkach, *Magnetocumulative Generators*. New York, NY: Springer, 2000, ISBN: 978-1-4612-7053-9. DOI: 10.1007/978-1-4612-1232-4.

[13] S. I. Shkuratov, E. F. Talantsev, J. Baird, L. L. Altgilbers, and A. H. Stults, "Explosive-driven mini-system based on shock wave ferromagnetic seed source and loop magnetic flux compression generator," in *PPPS-2007 - Pulsed Power Plasma Science 2007*, vol. 2, 2007, pp. 1141–1145, ISBN: 1-4244-0914-4. DOI: 10.1109/PPPS.2007.4652389.

[14] P. Appelgren, *Experiments with and modelling of explosively driven magnetic flux compression generators*. School of Electrical Engineering, Physical Electrotechnology, Kungliga Tekniska högskolan (KTH), 2008, ISBN: 978-91-7415-174-9.

[15] S. Lukasik, G. Zepko, and R. Jameson, "Magnetic-Flux Compression in an Explosion Geometry," English, in *Proceedings of the Conference on Megagauss Magnetic Field Generation by Explosives and Related Experiments*, Frascati, Italy: European Atomic Energy Community (Euratom), Sep. 1965, pp. 397–419.

[16] R. S. Caird, D. J. Erickson, C. M. Fowler, B. L. Freeman, and J. H. Goforth, "A circuit model for the explosive-driven plate generator," English, Los Alamos National Lab, Tech. Rep., 1983. [Online]. Available: https://digital.library.unt.edu/ark:/67531/metadc1107244/.

[17] H. H. Woodson and J. R. Melcher, *Electromechanical Dynamics*. Krieger Publishing Company, 1968, ISBN: 9780894644597 (v.1), 9780898748475 (v. 2), 9780898748482 (v. 3).

[18] A. Peirce. (Dec. 2017). Heat conduction with time dependent boundary conditions using Eigenfunction Expansions, [Online]. Available: https://www.math.ubc.ca/~peirce/M257_316_2012_Lecture_20.pdf (visited on 09/03/2019).

[19] J. Kennedy, "GURNEY ENERGY OF EXPLOSIVES: ESTIMATION OF THE VELOCITY AND IMPULSE IMPARTED TO DRIVEN METAL," Sandia Laboratories, Albuquerque, New Mexico 87115, SC-RR-70-790, Dec. 1970, p. 39.

[20] (2020). Overview of materials for brass. English, [Online]. Available: http://www.matweb.com/search/DataSheet.aspx?MatGUID=d3bd4617903543ada92f4c101c2a20e5 (visited on 01/02/2020).

[21] C. M. Fowler, W. B. Garn, and R. S. Caird, "Production of very high magnetic fields by implosion," *Journal of Applied Physics*, vol. 31, no. 3, pp. 588–594, Mar. 1960, ISSN: 0021-8979, 1089-7550. DOI: 10.1063/1.1735633. [Online]. Available: http://aip.scitation.org/doi/10.1063/1.1735633 (visited on 11/23/2019).

[22] (2019). Oxygen-free electronic Copper, UNS C10100. English, [Online]. Available: http://www.matweb.com/search/datasheetText.aspx?bassnum=MC101A (visited on 12/09/2019).

[23] "Military explosives," DEPARTMENT OF THE ARMY, TM 9-1300-214, Sep. 1984, p. 355.

[24] W. P. Walters and J. A. Zukas, *Fundamentals of Shaped Charges*. John Wiley & Sons, Inc., 1989, 412 pp., ISBN: 0-471-62172-2.

[25] A. I. Pavlovskii, R. Z. Lyudaev, L. I. Sel'Chenkov, A. S. Seryoghin, V. A. Zlotov, A. S. Yuryzhev, D. I. Zenkov, V. Y. Gurin, A. S. Boriskin, and V. F. Basmanov, "A multiwire helical magnetic cumulation generator," in *Megagauss Physics and Technology*, Springer US, 1980, pp. 585–593. DOI: 10.1007/978-1-4684-1048-8_54.

[26] S. I. Shkuratov, E. F. Talantsev, J. C. Dickens, M. Kristiansen, and J. Baird, "Longitudinal-shock-wave compression of nd2fe14b high-energy hard ferromagnet: The pressure-induced magnetic phase transition," *Applied Physics Letters*, vol. 82, no. 8, pp. 1248–1250, Feb. 24, 2003, ISSN: 0003-6951, 1077-3118. DOI: 10.1063/1.1554486. [Online]. Available: http://aip.scitation.org/doi/10.1063/1.1554486 (visited on 12/12/2019).

[27] J. Wei, S. Ma, P. Liu, and Y. Shi, "Demagnetization process analysis and numerical simulation of magnet with shock wave from compact explosively driven ferromagnetic generator," *IOP Conference Series: Materials Science and Engineering*, vol. 428, p. 012 014, Oct. 1, 2018, ISSN: 1757-899X. DOI: 10.1088/1757-899X/428/1/012014. [Online]. Available: http://stacks.iop.org/1757-899X/428/i=1/a=012014?key=crossref.1e33c5fee825f3e76416226080a7760e (visited on 12/12/2019).

[28] C. Hoberman, "Radial expansion/retraction truss structures," pat. 5 024 031, Jun. 18, 1991.

[29] S. Pellegrino, *Deployable structures*, en, ser. Courses and lectures / International Centre for Mechanical Sciences 412. Wien: Springer, 2001, OCLC: 248341093, ISBN: 978-3-211-83685-9.

[30] C. R. Paul, *Inductance: loop and partial*. Hoboken, N.J.: Wiley ; IEEE, 2010, 379 pp., OCLC: ocn428031806, ISBN: 978-0-470-46188-4.

[31] R. Dengler, "Self inductance of a wire loop as a curve integral," *Advanced Electromagnetics*, vol. 5, no. 1, p. 1, Jan. 29, 2016, ISSN: 2119-0275. DOI: 10.7716/aem.v5i1.331. [Online]. Available: http://www.aemjournal.org/index.php/AEM/article/view/331 (visited on 11/23/2019).